Available online at www.sciencedirect.com
ScienceDirect
Acta Materialia 59 (2011) 6187–6204
Acta MATERIALIA
www.elsevier.com/locate/actamat

Precipitates in Al–Cu alloys revisited: Atom-probe tomographic experiments and first-principles calculations of compositional evolution and interfacial segregation

Aniruddha Biswas [a,b], Donald J. Siegel [c,d,*], C. Wolverton [a], David N. Seidman [a,e]

[a] Department of Materials Science and Engineering, Northwestern University, 2220 Campus Drive, Evanston, IL 60208, USA
[b] Materials Science Division, Bhabha Atomic Research Centre, Mumbai 400 085, India
[c] Mechanical Engineering Department, University of Michigan, 2350 Hayward St., Ann Arbor, MI 48109-2125, USA
[d] Applied Physics Program, University of Michigan, 2350 Hayward St., Ann Arbor, MI 48109-2125, USA
[e] Northwestern University Center for Atom-Probe Tomography, Northwestern University, Evanston, IL 60208, USA

Received 3 May 2011; received in revised form 8 June 2011; accepted 18 June 2011
Available online 19 July 2011

Abstract

Atom-probe tomography, transmission electron microscopy, X-ray diffraction and first-principles calculations are employed to study: (i) compositional evolution of GPII zones and θ' precipitates; and (ii) solute segregation at α-Al/θ' interfaces in Al–1.7 at.% Cu (Al–4 wt.% Cu) alloys. GPII zones are observed after aging at 438 K for 8 h, whereas higher aging temperatures, 463 K for 8 h and 533 K for 4 h, reveal only θ' precipitates. Most GPII zones and θ' precipitates are demonstrated to be Cu-deficient at the lower two aging temperatures; only the 533 K treatment resulted in θ' stoichiometries consistent with the expected Al_2Cu equilibrium composition. For alloys containing ~200 at. ppm Si we find evidence of Si partitioning to GPII zones and θ' precipitates. Significant Si segregation is observed at the coherent α-Al/θ' interface for aging at 533 K, resulting in an interfacial Si concentration more than 11 times greater than in the α-Al matrix. Importantly, the Si interfacial concentration undergoes a transition from a non-equilibrium delocalized profile to an equilibrium localized profile as the aging temperature is increased from 463 to 533 K. Consistent with these measurements, first-principles calculations predict a strong thermodynamic driving force favoring Si partitioning to Cu sites in θ'. Silicon segregation at, and partitioning to, θ' precipitates results in a decrease in interfacial free energy, and concomitantly an increase in the nucleation current. Our results suggest that Si catalyzes the early stages of precipitation in these alloys, consistent with the higher precipitate number densities observed in commercial Al–Cu–Si alloys.

Keywords: Three-dimensional atom probe; First-principles electron theory; Interface segregation; Precipitation; Aluminum alloys

1. Introduction

The binary Al–Cu system is a well-studied precipitation strengthening system because it forms the basis for a wide range of age-hardening alloys that are technologically important. The precipitation sequence observed on aging these alloys, GPI → GPII(θ'') → θ' → θ, is often used as a model system for describing the fundamentals of precipitation hardening [1]. This sequence commences with the formation of coherent GPI and GPII zones. GPI zones are described as consisting of single layers of pure Cu atoms on $\{0\,0\,1\}_{\alpha\text{-Al}}$ planes. An accepted structural model of GPII consists of two Cu $\{0\,0\,2\}$ layers separated by three Al planes [2,3], with the stoichiometry Al_3Cu. First-principles calculations [4] also strongly support these structural models. Metastable θ', the main strengthening phase, has a body-centered tetragonal crystal structure with the stoichiometry Al_2Cu [5,6]. The precipitation sequence ends

* Corresponding author at: Mechanical Engineering Department, University of Michigan, 2350 Hayward St., Ann Arbor, MI 48109-2125, USA.
E-mail address: djsiege@umich.edu (D.J. Siegel).

1359-6454/$36.00 © 2011 Acta Materialia Inc. Published by Elsevier Ltd. All rights reserved.
doi:10.1016/j.actamat.2011.06.036

with the transformation of the θ' phase to the incoherent equilibrium θ phase, Al_2Cu, that possesses a tetragonal C16 crystal structure.

Given its importance for strengthening Al, a large number of studies of the Al–Cu precipitation sequence have focused on the properties of metastable θ' precipitates [7–11]. These precipitates exhibit a high-aspect-ratio plate-like morphology with coherent $(0\,0\,1)\ \theta' \| \{0\,0\,1\}_{\alpha\text{-Al}}$ interfaces parallel to their broad faces and semi-coherent interfaces at their peripheries [7]. This morphology is often rationalized by a large anisotropy in the interfacial free energy (γ) and elastic strain energies between the coherent and semi-coherent interfaces, with the broad coherent interfaces possessing a smaller γ value than the semi-coherent interfaces. Aaronson et al. [8,9] estimated the interfacial energy anisotropy factor to be ~12. Recent first-principles calculations, which decoupled the contributions of interfacial and elastic-strain energies, reported an anisotropy factor of ~3 [10,11].

The increasing use of Al–Cu alloys in commercial applications (e.g. cast 319 alloys for automobile engine blocks) continues to drive further studies of the properties of θ' precipitates [12–18]. Relatively little is known, however, concerning the compositional evolution of θ' precipitates since its nanometer-scale platelet-like morphology makes quantitative analytical electron microscopy analyses extremely difficult. This is reflected in the scant literature on solute-atom segregation at the platelets's cores and at the α-Al matrix/precipitate interfaces. This dearth of information is unfortunate since this data is essential for the development of accurate models of precipitation kinetics and strengthening. For example, segregation at interfaces is a result of a decrease in γ, which leads to a Gibbsian interfacial excess of solute (Γ) and retards precipitate coarsening. Moreover, deviations from the expected precipitate stoichiometry, in the form of excess concentrations of solute in the precipitate core, may indicate the existence of heterogeneous nucleation [19] and identify mechanisms that limit the coarsening rate. Since commercial process optimization tools rely upon accurate predictions of alloy microstructure as a function of processing conditions, it is desirable to understand and quantify the impact of nanoscale chemical composition on precipitation kinetics.

Three-dimensional (3-D) atom-probe tomography (APT) is capable of addressing these issues [20], and is currently the most suitable instrument at the subnano- to nano-scale for studying the compositions of nanoscale θ' platelets and their heterophase interfaces with the α-Al matrix. Prior evidence for magnesium segregation at coherent α-Al/$Al_3Sc(L1_2)$ heterophase interfaces, utilizing APT, demonstrates the power of this approach for measuring small values of Γ [19]. Nevertheless, prior APT studies of precipitation in Al–Cu-based alloys by different groups have reported differing results [21–25]. For instance, Karlik et al. [23] have summarized the conflicting results [21,22] pertaining to the compositions of GP zones. Additionally, Shollock et al. [24] and Sano et al. [25] performed APT analyses of θ' precipitates in Al–1.7Cu–0.34 Mg–0.1Ag at.% and Al–2.7Cu–0.5 Mg–0.1Ag–0.26Mn–0.04Zr at.% alloys, respectively, and reported different Cu concentrations for the θ' phase. Shollock et al. [24] obtained an Al_3Cu stoichiometry for the θ' phase, whereas Karlik et al. [23] found a stoichiometry of Al_2Cu. Furthermore, there have been relatively few APT studies of the temporal evolution of θ' platelets, with the majority of studies focusing on precipitate nucleation. Employing atom-probe field-ion microscopy and APT, respectively, Ringer et al. [26] and Honma et al. [27] investigated whether trace additions of tin could enhance θ' nucleation. Similarly, little is known regarding solute interfacial segregation in Al–Cu alloys: Cu segregation at a small-angle grain boundary has been studied in thin films [28], and Srivastava et al. [29] studied segregation at equilibrium θ precipitates.

In view of the above, the objective of this work is to study the nanoscale chemical composition in the Al–Cu precipitation sequence, and to elucidate whether these compositional differences correlate with variations in the observed precipitation kinetics. Specifically, using a combination of 3-D local-electrode atom-probe (LEAP) tomography, X-ray diffraction (XRD), transmission electron microscopy (TEM) and first-principles calculations, we examine: (i) the compositional evolution of GPII zones and θ' platelets; and (i) Si solute segregation at coherent α-Al/ θ' interfaces in Al–1.7 at.% Cu (Al–4 wt.% Cu), with ~200 at. ppm additions of Si. The ternary Al–Cu–Si system was studied to clarify the role of Si in the faster precipitation kinetics observed in commercial Si-containing 319 alloys [30]. For aging at 438 and 463 K, our analyses reveal clear evidence of significant partitioning of Si at the cores of the GPII zones and θ' precipitates, consistent with Si playing a catalytic role in nucleating these phases. At 533 K, the Si core concentration of θ' decreases in favor of forming a Si-rich, localized segregation profile at the coherent α-Al/θ' interface. We quantify this segregation with the relative Gibbsian interfacial Si excess, and use this data to estimate the segregation-induced reduction of interfacial free energy. Additionally, first-principles calculations of solute substitutional energies and partitioning behavior provide energetic explanations for the experimentally measured phenomena.

2. Methodologies

2.1. Experimental methods

Aluminum (ALCOA) of two different purities was used in conjunction with high-purity (99.99%) Cu (Alfa Aesar) to prepare Al–1.7 at.% Cu (Al–4 wt.% Cu) specimens. The first Al source was 99.99% pure, while the second source contained two main impurities, ~216 at. ppm Si and ~267 at. ppm Fe. These alloys were melted in an alumina crucible in a resistance-heated furnace and directionally solidified in a graphite mold. The high-purity Al alloy

Table 1
Chemical analyses of the alloys.

Si (wt.%)	Cu (wt.%)	Fe (wt.%)
Alloy A		
0.0012 (0.0011 at.%)	4.0 (1.74 at.%)	0.0004 (0.0002 at.%)
Alloy B		
0.022 (0.0216 at.%)	4.0 (1.74 at.%)	0.054 (0.0267 at.%)

is denoted alloy A and the second ("impure") one alloy B. Table 1 presents the results of the chemical analyses performed by Shiva Technologies Inc. (Syracuse, NY). The cast samples were homogenized in air at 758 K for 24 h, followed by water quenching. They were subsequently aged in air at one of three different temperatures, 438, 463 and 533 K (165, 190 and 260 °C) for 8, 8 and 4 h, respectively. These aging conditions were chosen to study the temporal evolution of the precipitation sequence from GPII to θ'.

After the aging treatments the samples were characterized using a conventional Rigaku X-ray diffractometer with Cu Kα radiation at Northwestern University, and with synchrotron radiation at the Advanced Photon Source (APS) at the Argonne National Laboratory, using the Dow–Northwestern–DuPont beam line. Synchrotron radiation with an energy of 17.477 keV and a wavelength of 0.0709 nm was utilized; the samples were polished to a flatness of 1 μm.

Specimens for TEM were prepared by punching discs with a 3 mm diameter from thin foils with a thickness of ~200 μm, followed by jet polishing with a Struers Tenupol-5 at −40 °C, using a 5 vol.% perchloric acid in a methanol electrolyte. TEM was performed employing an Hitachi 8100 microscope at 200 kV.

APT sample blanks with a square cross-sectional area of approximately 300 × 300 μm^2 and a 1 cm length were prepared by a combination of slicing and mechanical grinding [31,32]. A two-step electropolishing procedure was used for making tips from these blanks. A 10 vol.% perchloric acid in methanol solution was used for coarse polishing, and the final polishing was performed using a solution of 2 vol.% perchloric acid in butoxyethanol.

APT experiments were performed in either the electrical or laser pulsing modes using a Cameca (formerly Imago Scientific Instruments, Madison, WI) LEAP tomograph [33–40] in the Northwestern University Center for Atom-Probe Tomography (NUCAPT). APT data collection using the electrical pulsing mode was performed at a specimen temperature of 30 ± 0.3 K, with a voltage pulse fraction (pulse voltage/steady-state DC voltage) of 20%, a pulse repetition rate of 200 kHz and a background gauge pressure of $<6.7 \times 10^{-8}$ Pa (5×10^{-10} torr). For picosecond laser (wavelength = 532 nm) pulsing, a pulse repetition rate of 500 kHz was utilized, with the specimen maintained at 30 ± 0.3 K. Additionally, we performed a series of experiments that involved varying the laser energy per pulse from 0.5 to 4 nJ, and observed no measureable effect of laser beam heating of the wire tips because of its high thermal diffusivity. Therefore, we used a laser energy of 2 nJ per pulse, which facilitates collecting datasets of ~10^7–10^8 atoms per specimen.

Care was taken to establish the equivalence of electrical and laser pulsing, using the same sample. The average detection rate ranged from 0.04 to 0.08 ions pulse^{-1} for the APT analyses. The LEAP tomographic data were analyzed employing IVAS 3.0 (Cameca, Madison, WI). The α-Al/θ' interfaces were delineated with 3.5 at.% Cu isoconcentration surfaces for samples aged at 438 K, and 9 at.% Cu isoconcentration surfaces for samples aged at 463 or 533 K. Efficient sampling procedures [41] were used to generate these isoconcentration surfaces. The parameters employed for the isoconcentration surfaces are: (i) voxel size = 1 × 1 × 1 nm^3; (ii) delocalization distance = 3 nm; and (iii) sample count threshold = 3%. Compositional information as a function of depth was obtained with: (i) 1-D concentration profiles through the regions of interest; and (ii) the proximity histogram method [42]. All error bars correspond to two standard deviations from the mean value for the compositional analyses. The counting statistics error, $1/\sqrt{N}$, was used for the number density calculation, where N is the total number of θ' platelets. Additional details concerning experimental and analysis procedures are given elsewhere [19,43].

2.2. Computational methods

The energies for Si segregation at coherent and semi-coherent α-Al/θ' interfaces, ΔE_{seg} [44], were evaluated using first-principles calculations based on the PW91 generalized gradient approximation [45] to density functional theory [46–47], as implemented in the Vienna Ab-initio Simulation Package [48]. The projector augmented wave method [49–50] was used to describe the core–valence electron interaction, and tests were performed to ensure that **k**-point sampling density was sufficient to ensure that segregation energies converged to ~0.02 eV per solute atom. A 300 eV cutoff energy was used for the plane-wave basis.

Segregation was modeled at coherent and semi-coherent α-Al matrix/ θ ′ precipitate interfaces using distinct interfacial supercells (Fig. 1). Both models adopt the experimental matrix/precipitate orientation relationship $(0\,0\,1)_{\theta'}\|\{0\,0\,1\}_{Al}$ and $[0\,1\,0]_{\theta'}\|[0\,1\,0]_{Al}$ [13], which and are based on earlier models [10,11]. The coherent system is representative of the interface at the broad flat faces of the θ' platelet, which exhibits a small misfit strain of 0.7%, as $a_{\theta'} \approx a_{Al}$. Our model cell consists of two symmetry-equivalent Al/θ' interfaces separated by seven planes of Al-{0 0 1} and nine planes of θ', for a total of 108 atoms. Prior studies indicate that slabs of this thickness yield converged interfacial properties [51]. To minimize solute–solute image interactions, the dimensions of the supercell parallel to the interfacial plane (cell vectors **a** and **b**) were expanded, resulting in a 2 × 2 geometry with dimensions $|\mathbf{a}| = 2a_{\theta'}$ and $|\mathbf{b}| = 2a_{\theta'}$.

The semi-coherent model (Fig. 1, bottom panel) captures the interfacial properties at the periphery of the θ'

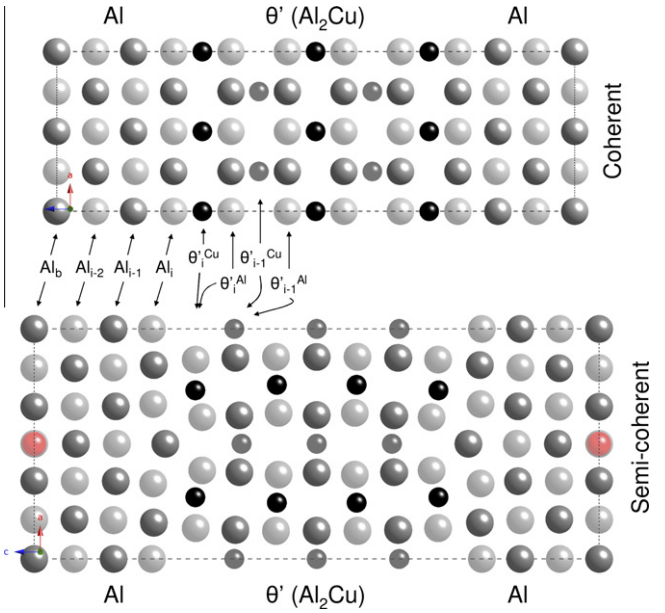

Fig. 1. Relaxed supercells used for the Al/θ'interfacial segregation calculations. Top: coherent interface; bottom: semi-coherent interface. Al atoms are grey, Cu atoms are black; shading is used to convey the position relative to the plane of the page. The red atom in the semi-coherent supercell illustrates the position of a solute at a bulk-like site in the Al matrix. (Sub)lattice planes are labeled according to their position relative to the interface planes. For example: "Al_i" identifies the Al plane adjacent to the interface; "Al_b" refers to a bulk-like plane in the Al matrix; "θ'^{Cu}_i" refers to the interfacial Cu layer within the θ' precipitate. Note that in the semi-coherent interface Al and Cu sites within θ' can reside in the same planes parallel to the interface. (For interpretation of the references to colour in this figure legend, the reader is referred to the web version of this article.)

platelets. Unlike the coherent system, the semi-coherent interface must accommodate a 42% lattice-parameter mismatch between a_{Al} and $c_{\theta'}$ along one direction (cell vector **a**) in the interfacial plane. This misfit is minimized utilizing a semi-coherent geometry [11] with $|\mathbf{a}| = 2c_{\theta'} \approx 3a_{Al}$, yielding a −5.1% misfit. In the orthogonal interfacial direction, **b**, the misfit is the same as in the coherent system, 0.7%, and we apply a double-cell geometry, $|\mathbf{b}| = 2a_{\theta'}$. In the **c**-direction (normal to the interface) seven {1 0 0} layers of Al and θ' separate two symmetry-equivalent interfaces, resulting in a total of 168 atoms.

In both interface models the magnitude of the supercell vector, |**c**|, normal to the interfacial plane was optimized by minimizing the total energy of the "clean" interface (no solute atoms) with respect to cell length, while allowing for the simultaneous relaxation of atomic positions. All segregation calculations were performed using these fixed cell parameters. Additionally, atomic positions were relaxed such that residual forces on all atoms were <0.02 eV Å^{-1}.

In addition to these interfacial calculations, a series of bulk calculations were performed to estimate 0 K point-defect formation energies and the relative heats of solution for substituting Si solute atoms in the Al matrix and θ' precipitates. The defect energies are those for vacancy and anti-site formation within the bulk θ' phase. These were evaluated using a $2 \times 2 \times 2$ supercell containing 96 atoms (95 for a vacancy calculation). Calculations of the Si heat of solution in θ' were performed using a $2 \times 2 \times 2$ supercell. A $4 \times 4 \times 4$ cell (256 atoms) was used to study the energetics of Si insertion into bulk Al. All bulk calculations included relaxation of internal atomic positions, while keeping the external cell parameters fixed. Energies were converged with respect to **k**-point sampling to better than 1 meV atom^{-1}.

3. Results

3.1. X-ray analyses: identity of the precipitates

Fig. 2a–d displays XRD powder patterns of the Al–Cu alloys in the solutionized or solutionized plus aged conditions. Solutionized samples of both alloys were found to be single-phase solid solutions of Cu in α-Al (Fig. 2a). For aging at 438 or 463 K, conventional XRD experiments did not exhibit extra reflections corresponding to a second phase. Synchrotron radiation experiments on these samples yielded XRD patterns consistent with the presence of GPII zones and/or θ' platelets (see below). GPII zones nominally have a tetragonal crystal structure, with lattice parameters $a = b = 0.404$ nm, $c = 0.768$ nm [3,21]. The θ' phase is also tetragonal, with lattice parameters $a = b = 0.404$ nm, $c = 0.58$ nm [6]. These lattice parameters were used to calculate the planar spacings of the GPII zones and θ' phases. Fig. 2b displays XRD patterns for samples aged at 438 K for 8 h. The two extra peaks at 2θ values of 14.75° and 36.07° belong to GPII zones and are indexed as the (1 1 0) and (2 2 4) reflections, respectively, which are highlighted in the insets. Since the d-spacings of the (1 1 0) planes of θ' and GPII are identical, no conclusive evidence for the presence of θ' platelets was detected using XRD for samples aged at 438 K. Alternatively, samples aged at 463 K for 8 h and analyzed using synchrotron radiation exhibit evidence for θ' platelets (Fig. 2c). The extra peak observed at $2\theta = 23.75°$ is the (1 2 1) reflection of the θ' phase, as highlighted in the inset. Finally, θ' platelets are visible for the 533 K for 4 h aging treatment: Fig. 2d and its inset present XRD patterns with the (1 0 1) peak of the θ' phase highlighted. No peak corresponding to GPII zones is detected after aging either at 463 K for 8 h or at 533 K for 4 h.

3.2. TEM analyses

TEM analyses of the aged alloys (Fig. 3) were found to be consistent with the XRD studies. GPII platelets are observed in samples aged at 438 K for 8 h, as shown in the ⟨1 0 0⟩ zone bright-field micrograph in Fig. 3a. The ⟨1 0 0⟩ streaking associated with the GPII platelets is observed in the corresponding diffraction pattern. θ' platelets are detected in samples aged at 463 K for 8 h or 533 K for 4 h, as displayed in the ⟨1 0 0⟩ zone bright-field micro-

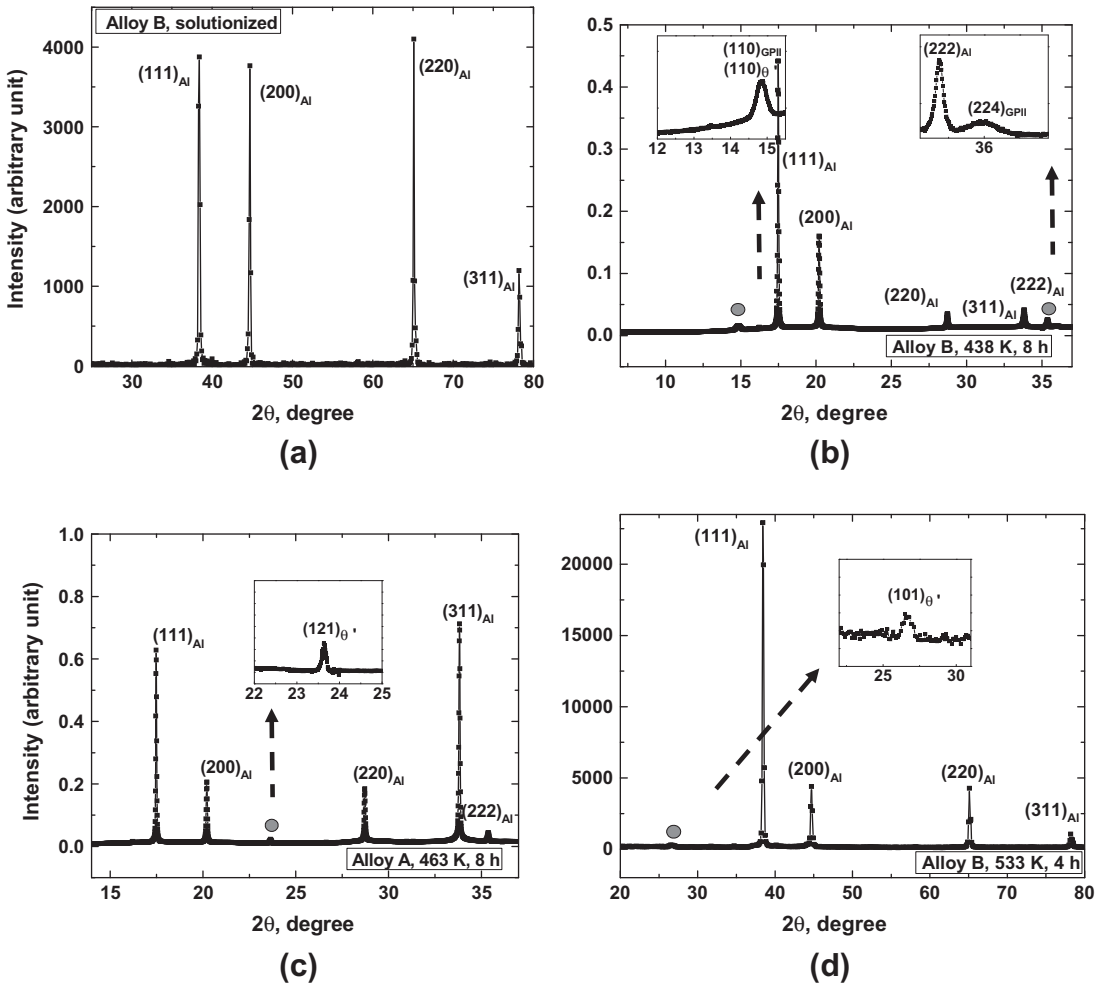

Fig. 2. (a) Solutionized samples showing a single-phase solid solution of copper in α-Al; (b–d) representative diffraction patterns for samples aged at (i) 438 K for 8 h, (ii) 463 K for 8 h and (iii) 533 K for 4 h, respectively. The insets highlight the reflections from the precipitates. (a and d) were obtained using a conventional diffractometer; synchrotron radiation was used for (b) and (c).

graphs of Fig. 3b and c. No GPII zones were detected in samples aged at the two higher temperatures.[1]

3.3. LEAP tomographic analyses: mass spectra, microstructure and composition

Fig. 4a and b compares the relevant portions of the mass-to-charge state (m/n) spectra obtained using electrical or laser pulsing. Aluminum occurs in the singly charged ($^{27}Al^{1+}$) and doubly charged ($^{27}Al^{2+}$) states, but the Al hydrides ($^{27}Al^{1}H^{+}$, $^{27}Al^{1}H_{2}^{+}$) that appear due to the presence of residual hydrogen in the ultrahigh-vacuum sample chamber are always singly charged. The two Cu isotopes ($^{63}Cu^{1+}$ and $^{65}Cu^{1+}$, not displayed) and their hydrides are also present in the singly charged state. Of particular concern is Si, whose major isotope in the singly charged state ($^{28}Si^{1+}$) may coincide with the singly charged Al hydride peak ($^{27}Al^{1}H^{+}$). We find that laser pulsing using 2 nJ pulse^{-1} results in Si being evaporated only in the doubly charged state ($^{28}Si^{2+}$). This, and the absence of a doubly charged Al hydride peak, permits us to measure the bulk Si concentration utilizing the doubly charged Si peak at an m/n value of 14 (Fig. 4a). Neither the singly charged Al hydride peaks nor the $^{28}Si^{2+}$ peak can be resolved employing electrical pulsing. Furthermore, the proportion of $^{27}Al^{2+}$ in the mass spectra is small employing laser pulsing, presumably because of the smaller standing dc voltage. We therefore conclude that picosecond laser pulsing yields better mass resolving power ($m/\Delta m$) than does electrical pulsing.

None of the four isotopes of the impurity element Fe (present in samples fabricated from alloy B) are detected in the mass spectra, either in the singly or doubly charged states, because Fe has a negligible solid solubility in Al (0.014 at. ppm at 503 K [52]). Iron, however, forms intermetallic compounds with Al and it is difficult to detect a

[1] Although only the (1 2 1) reflection is shown in Fig. 2c, synchrotron radiation was able to detect both the (1 2 1) and (1 0 1) reflections in this sample. A conventional X-ray diffractometer was used to analyze the 533 K aged sample shown in Fig. 2d. This technique was capable of detecting only the (1 0 1) reflection.

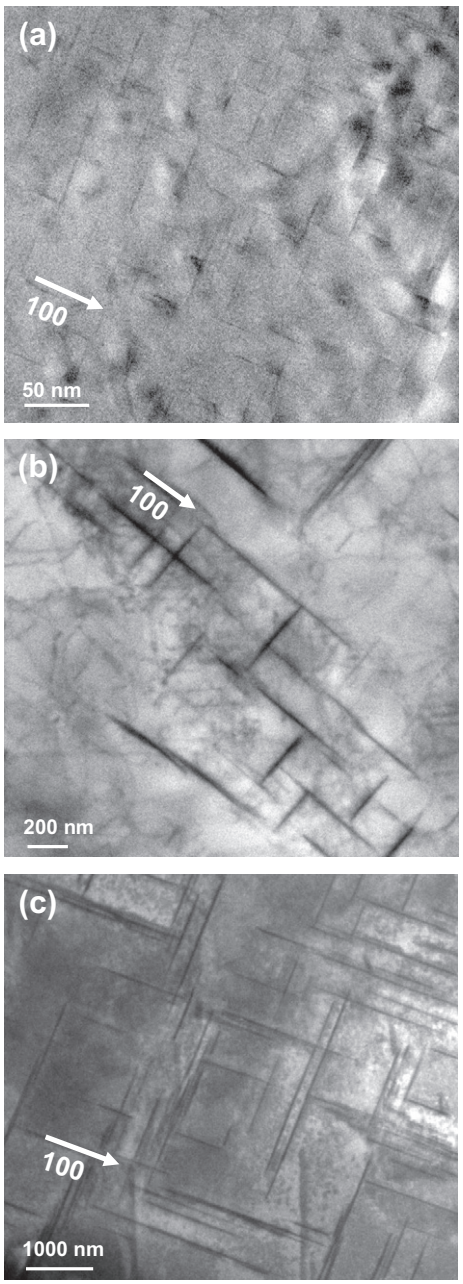

Fig. 3. (a) Bright-field transmission electron microscope micrograph depicting GPII platelets in the $\langle 1\,0\,0\rangle_{Al}$ zone obtained after aging at 438 K for 8 h; (b and c) the θ' precipitates in the $\langle 1\,0\,0\rangle_{Al}$ zone observed after aging at 463 K for 8 h (b) and 533 K for 4 h (c), respectively.

small-volume fraction of an Fe intermetallic phase(s) employing APT.

3.3.1. Aging at 438 K for 8 h

Consistent with the XRD and TEM measurements, thin GPII platelets are observed with APT in samples aged at 438 K for 8 h. The number density, N_v, of the GPII platelets in alloy A is $N_v = 1.77 \pm 0.1 \times 10^{22}\ m^{-3}$; electrical and laser pulsing experiments yield similar values of N_v. Fig. 5a exhibits a 3-D APT reconstruction of $\sim 9 \times 10^7$ atoms obtained from alloy A using electrical pulsing; only $\sim 10^5$

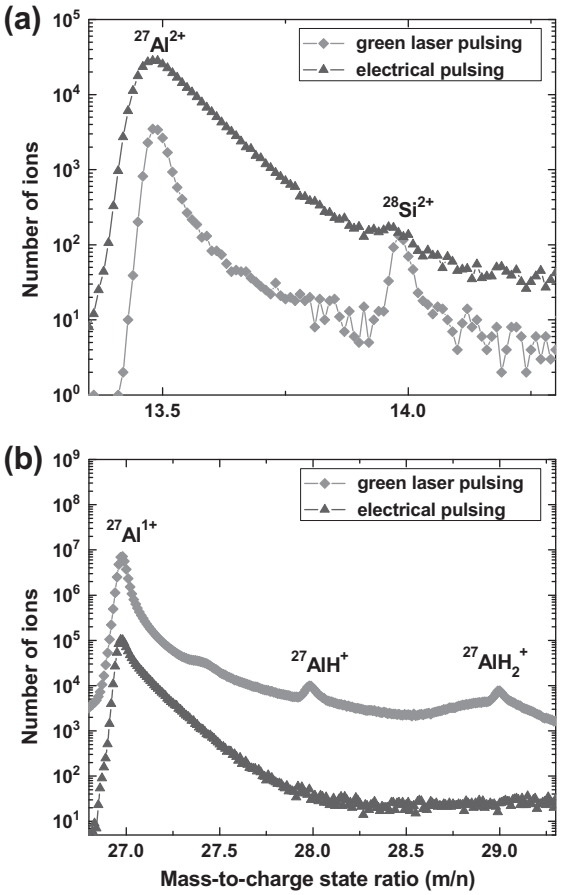

Fig. 4. Comparison of mass spectra obtained using electrical and laser pulsing. (a) Peaks for $^{27}Al^{2+}$ and $^{28}Si^{2+}$; (b) peaks for $^{27}Al^{1+}$, $^{27}AlH^{+}$ and $^{27}AlH_2^{+}$.

Cu atoms (red) are displayed. Fig. 5b displays a portion of this reconstructed volume containing a GPII platelet viewed edge-on. The same GPII platelet is visualized along a direction normal to the broad flat face of the platelet (Fig. 5c), along with its isoconcentration surface; only 20% of the Al (blue) atoms are displayed. Atomic planes of the α-Al matrix are visible in Fig. 5c, and their spacing matches the interplanar spacing of the {2 0 0} planes of Al (0.202 nm). The broad flat faces of the GPII platelets are parallel to {2 0 0} planes as GPII is coherent with the α-Al matrix, $\{2\,0\,0\}_{Al}$; these platelets are 2.02 ± 0.45 nm thick, with a diameter of 21.8 ± 3.1 nm.

The compositions of these GPII platelets were measured individually using a 1-D concentration profile along the axis of a cylinder placed perpendicular to each platelet (cylinder diameter: 7 nm; number of ions per step: 50; step size: ~0.04 nm). Fig. 6a demonstrates this for GPII platelets delineated by isoconcentration surfaces. A composition histogram (Fig. 6b) extracted from the same dataset for alloy A indicates a Cu concentration ranging from ~10 to 40 at.%, with the majority of precipitates exhibiting concentrations less than the GPII stoichiometry of 25 at.% Cu. GPII zones in alloy B (not displayed) exhibit a similar deficiency in Cu.

Alloy B exhibits a factor of three increase in the N_v value of GPII platelets ($5.67 \pm 0.1 \times 10^{22}\ m^{-3}$) with respect to

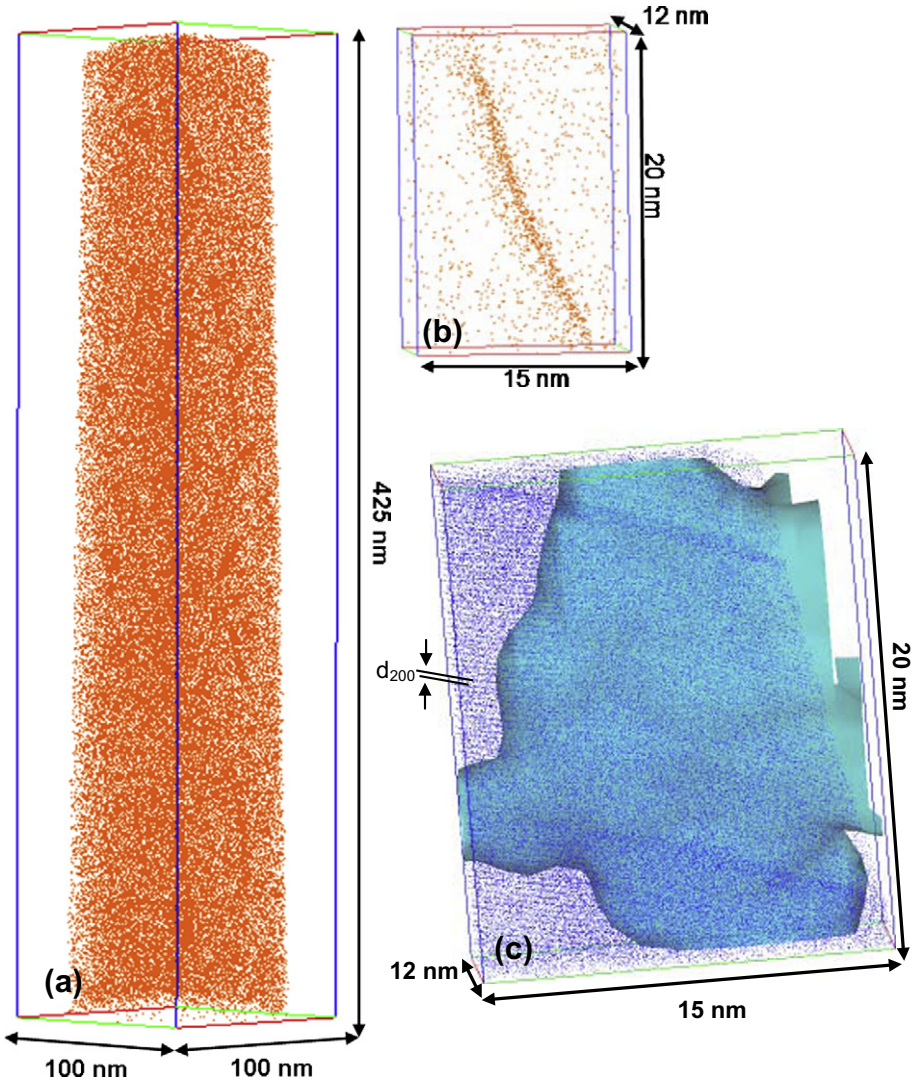

Fig. 5. 3-D reconstructions of a sample of alloy A aged 438 K for 8 h, obtained using electrical pulsing. Cu and Al atoms are displayed in red and blue, respectively. One GPII platelet is highlighted in (b); (c) shows that the {2 0 0} planes of Al are parallel to the broad face of the platelet. (For interpretation of the references to colour in this figure legend, the reader is referred to the web version of this article.)

alloy A. In further contrast to alloy A, the GPII platelets in the Si-containing alloy B display considerable Si partitioning relative to the α-Al matrix. The average Si concentration of 172 GPII platelets in alloy B is 0.107 ± 0.008 at.%, while the average Si concentration in the α-Al matrix is 0.0206 ± 0.002 at.%. Thus, the Si partitioning constant, the ratio of the Si concentration in GPII divided by its value in the α-Al matrix, is 5.19. The observation in alloy B of a larger N_V value, combined with the elevated concentrations of Si in GPII, suggests that Si plays a catalytic role in the heterogeneous nucleation of GPII platelets. A similar catalytic effect on the nucleation of Al_3Sc precipitates has been observed in Al–Sc alloys containing Si [53].

3.3.2. Aging at 463 K for 8 h

Aging for 8 h at 463 K yields thin and broad platelets of θ', as illustrated in 3-D reconstructions from alloys A (Fig. 7a) and B (Fig. 7b), where only Cu atoms (red) are displayed; in both of these cases, only 10% of the total Cu atoms detected are displayed. The datasets collected using electrical pulsing contain $\sim 1.6 \times 10^7$ atoms (Fig. 7a); those for laser pulsing contain $\sim 4.0 \times 10^7$ atoms (Fig. 7b). Synchrotron XRD experiments establish the existence of the θ' phase in these samples. Similar to GPII, the broad face of a θ' precipitate is coherent with $\{2\,0\,0\}_{\alpha\text{-Al}}$. The average precipitate thickness and diameter for 20 precipitates are 7.95 ± 1.47 nm and ~180 nm, respectively. The large diameter of the θ' platelets makes it impractical to report statistically significant differences in N_v between alloys A and B. Compared to the N_v value of GPII platelets in samples aged at 438 K, the $\theta' N_v$ value ($1.51 \pm 0.4 \times 10^{21}$ m^{-3}) is an order of magnitude smaller. Fig. 7c displays a 3-D reconstruction from alloy B, where θ' precipitates are delineated by 9 at.% Cu isoconcentration surfaces. This dataset contains $\sim 5.0 \times 10^7$ atoms and was obtained using laser pulsing.

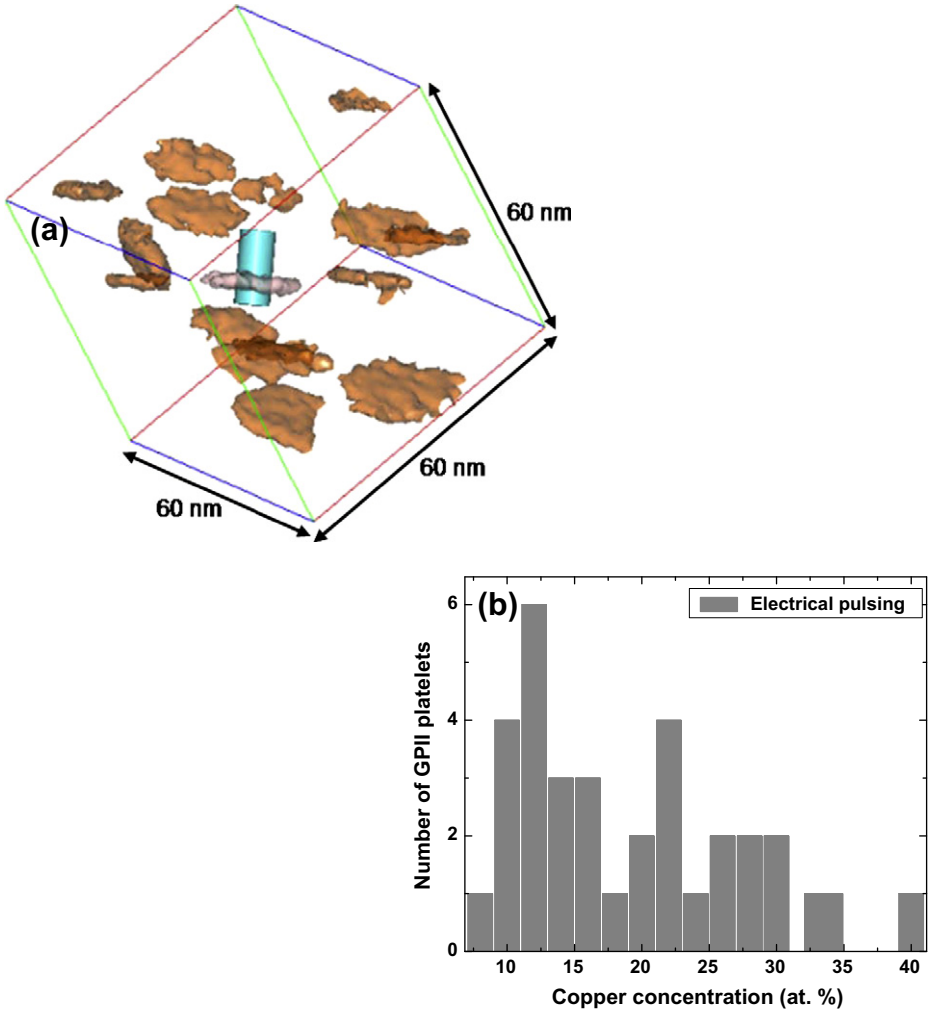

Fig. 6. (a) GPII platelets in alloy A imaged via APT after aging at 438 K for 8 h. The composition of each platelet was measured independently using a 1-D concentration profile along the cylinder. (b) Composition histogram showing a range of copper concentrations from ~10 to 40 at.% Cu.

To determine the concentration of Cu in the θ' core, a 1-D concentration profile was computed for the same 20 precipitates (alloy A) used to determine the precipitate dimensions. The Cu concentration ranges from 20.2 ± 2.7 to 35.28 ± 1.12 at.%, as demonstrated by the composition histogram (Fig. 7d). The equilibrium θ' stoichiometry is Al_2Cu, but the majority of the θ' precipitates for this aging condition are Cu deficient. Similar results for the Cu concentration were obtained for alloys A and B.

The proximity histogram (proxigram) method [41–42] was used for in-depth compositional analyses. Table 2 summarizes the compositions of the α-Al matrix and the θ' precipitates for a precipitate exhibiting a nearly stoichiometric Cu composition (Table 2, top panel) and a representative Cu-deficient θ' precipitate (Table 2, bottom panel), respectively. Notably, Si exhibits enhanced concentrations in both θ' precipitate types and is depleted in the α-Al matrix. The Si partitioning coefficients ($K_{si}^{\theta'/\alpha\text{-}Al}$) for these two types of θ' precipitates are 7.4 and 5.4, respectively. The Si partitioning coefficient is $K_{\mathrm{Si}}^{\theta'/\alpha-\mathrm{Al}} = \frac{c_{\mathrm{Si}}^{\theta'}}{c_{\mathrm{Si}}^{\alpha-\mathrm{Al}}}$, where $c_{\mathrm{Si}}^{\theta'}$ and $c_{\mathrm{Si}}^{\alpha-\mathrm{Al}}$ are the core concentrations of Si in the θ' precipitate and α-Al matrix, respectively.

3.3.3. Aging at 533 K for 4 h

The θ' platelets in samples aged at 533 K for 4 h are thicker and broader than those detected for the 463 K treatment. As the N_v value is also smaller by an order of magnitude (1.47×10^{20} m^{-3}), they become progressively more difficult to detect. The difference in N_v values of θ' precipitates between alloys A and B could not be ascertained for this aging condition due to poor statistics. A portion of a θ' precipitate from alloy B with a diameter of >200 nm and thickness of ~50 nm is displayed in Fig. 8. This dataset was collected using laser pulsing and contains $\sim 6.0 \times 10^7$ atoms; it exhibits a Cu core-concentration of 34.94 ± 1.2 at.%, which is close to the stoichiometric concentration (33.33 at.%). Concomitantly, there is a 50% reduction in the Si core concentration on aging at 533 K as compared to 463 K aging, which decreases from 0.103 ± 0.008 to 0.052 ± 0.015 at.% Si.

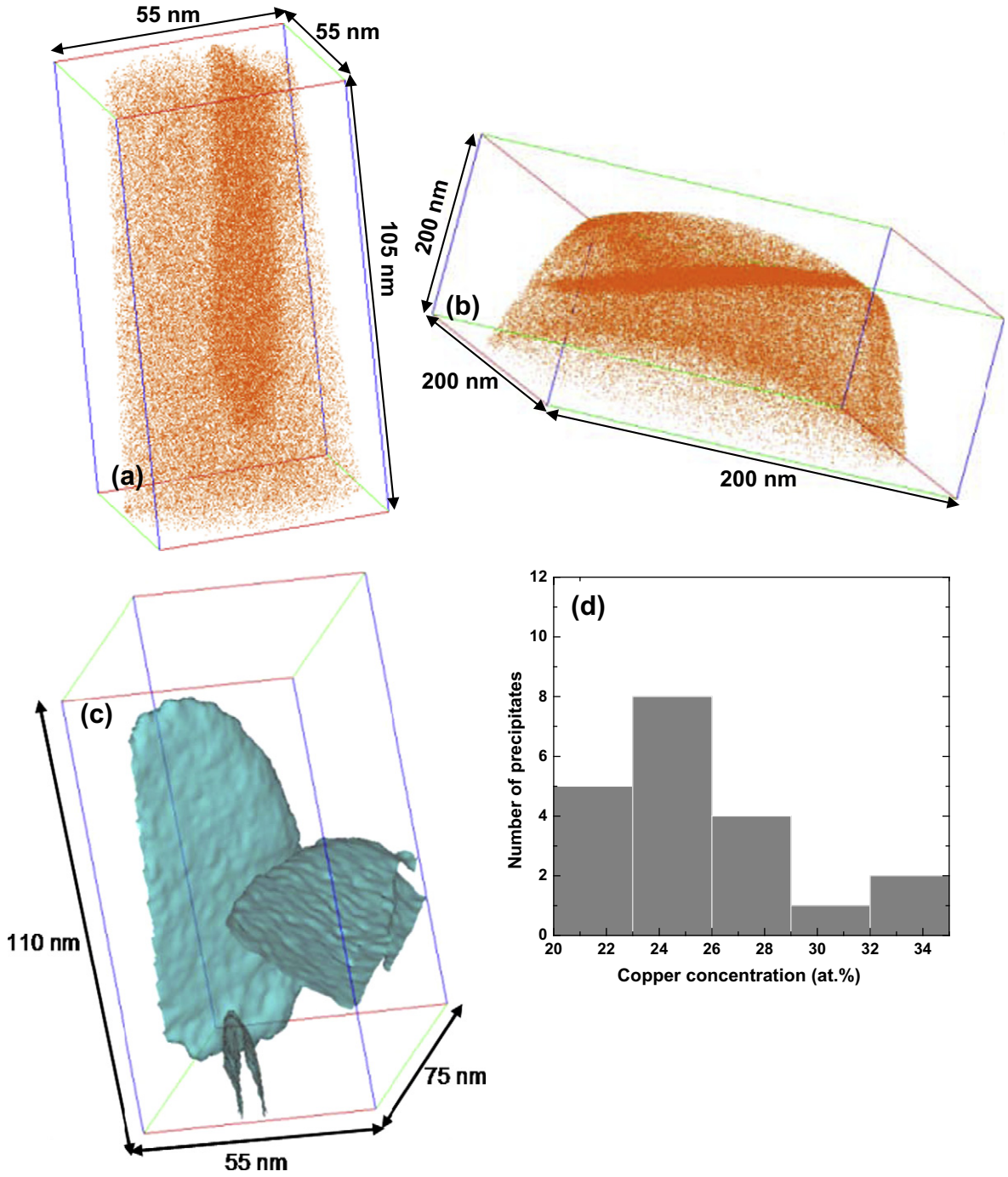

Fig. 7. Typical thin and large diameter platelet of θ' precipitate obtained after (a) aging alloy A and (b) alloy B at 463 K for 8 h. Only copper atoms (red) are displayed in (a) and (b). (c) θ' isoconcentration surfaces for alloy B. (d) Composition histogram for alloy A. (For interpretation of the references to colour in this figure legend, the reader is referred to the web version of this article.)

3.3.4. Heterophase interfacial segregation

Two sets of samples of alloy B, one aged at 463 K for 8 h and the other at 533 K for 4 h, were analyzed, with an emphasis on heterophase interfacial solute segregation at the coherent α-Al/θ' interface. Due to its small areal fraction, we were not able to capture similar data for the semi-coherent interface. Care was taken to choose θ' precipitates that were perpendicular to the analysis direction, due to the spatial depth resolution of 0.1 nm. The proxigram methodology [41,42] was used for this analysis (bin size of 0.7 nm; see Appendix A), where the concentration was measured with respect to distance from a 9 at.% Cu isoconcentration surface.

Fig. 9a and b displays a θ' platelet from a sample aged at 463 K for 8 h; it is perpendicular to the ⟨2 0 0⟩-type analysis direction and exhibits a Cu concentration close to the stoichiometric value (33.3 at.%). These interfaces are coherent with the α-Al matrix (Fig. 9c); its proxigram is

Table 2
Partitioning of alloying elements between the α-Al matrix and θ' precipitate after aging at 463 K for 8 h. Top rows: example of a nearly stoichiometric precipitate. Bottom rows: a representative Cu-deficient precipitate.

Element	α-Al matrix (at.%)	θ'-precipitate (at.%)
Nearly stoichiometric θ'-precipitate		
Al	99.52 ± 0.06	64.62 ± 1.12
Cu	0.47 ± 0.06	35.28 ± 1.12
Si	0.013 ± 0.006	0.096 ± 0.018
Typical Cu-deficient θ'-precipitate		
Al	99.19 ± 0.06	79.16 ± 0.6
Cu	0.782 ± 0.06	20.72 ± 0.6
Si	0.024 ± 0.01	0.129 ± 0.012

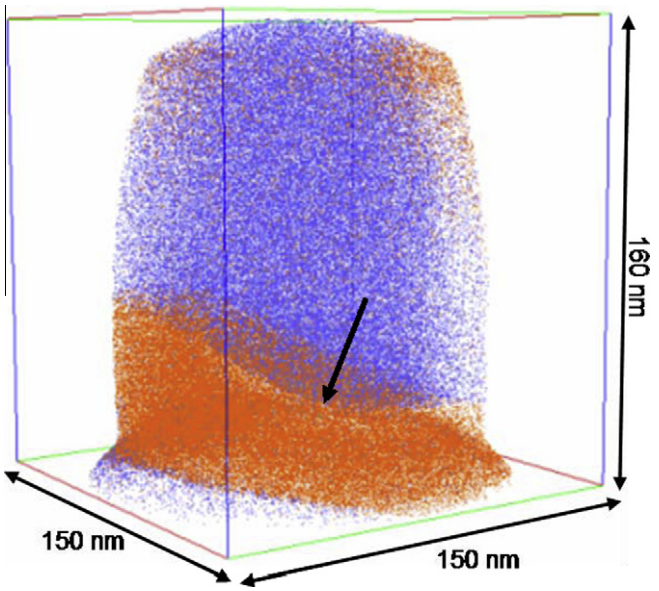

Fig. 8. θ' precipitate (indicated by arrow) obtained after aging alloy B at 533 K for 4 h, using green laser pulsing. Al atoms are represented in blue and Cu atoms in red. (For interpretation of the references to colour in this figure legend, the reader is referred to the web version of this article.)

displayed in Fig. 10. The solid vertical line indicates the location of the heterophase interface between the α-Al matrix and the θ' platelet, which is at the inflection point of the Al concentration profile. The spatial concentration profiles of the θ' platelet and α-Al matrix are displayed on the right- and left-hand sides of this line, respectively. No perceptible localized Si segregation in the vicinity of the α-Al/θ' coherent heterophase interface is detected. Analyses of Cu-deficient θ' platelets for the same aging condition reveals similar high Si concentrations at the precipitate core (Table 2, bottom panel), with no localized Si segregation at the coherent interface.

Fig. 11a and b displays a portion of the θ' platelet obtained after aging an alloy B specimen at 533 K for 4 h, and performing a similar analysis with the broad coherent face of the θ' platelet perpendicular to the analysis direction (⟨2 0 0⟩ type). The same values of the analysis parameters were used to create the isoconcentration surface (Fig. 11b). The proxigram calculated based on this

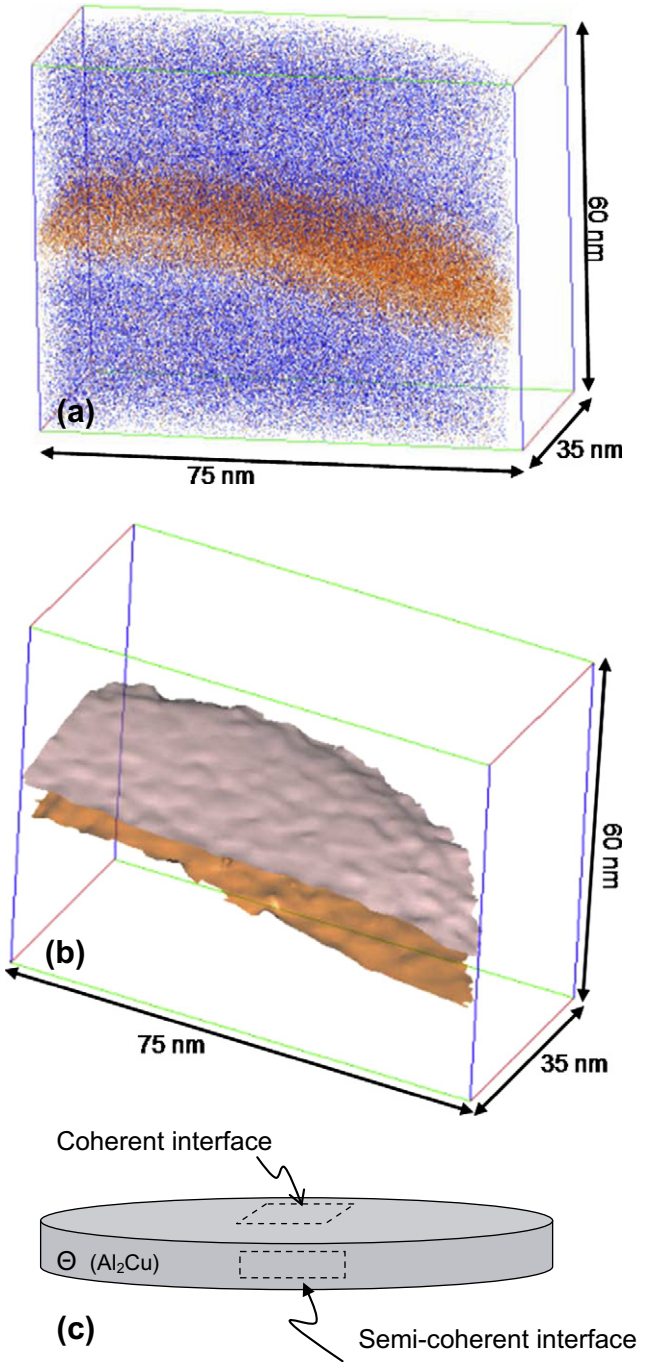

Fig. 9. (a) θ' precipitate from alloy B aged at 463 K for 8 h; (b) isoconcentration surfaces (9 at.% Cu) delineating the coherent matrix precipitate interface, as depicted in (c).

9 at.% Cu isoconcentration surface is displayed in Fig. 12. The striking result is definitive evidence for localized Si interfacial segregation at the coherent α-Al/θ' interface. The Si concentration at the interface is ~3 times the value observed in the core of the θ' platelet and is localized within 7.5 nm of the interface. Additionally, the majority of segregated Si is confined at the θ' side of the interface. As the magnitude of the Si concentration profile increases as the aging temperature is increased from 463 to 533 K, the

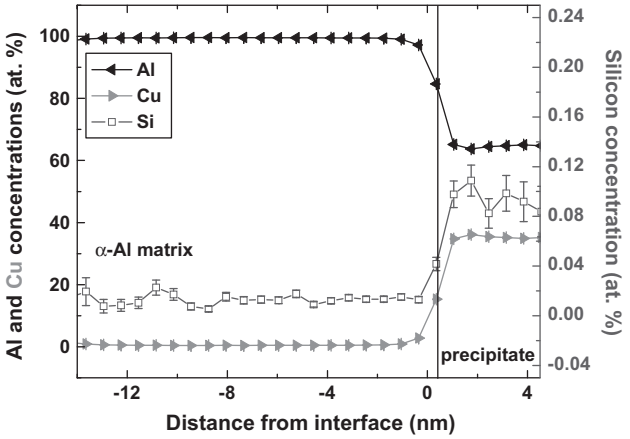

Fig. 10. Proxigram from a sample of alloy B aged at 463 K for 8 h. Green laser pulsing is used.

lower-temperature Si segregation profile is not in equilibrium.

The relative Gibbsian interfacial excess provides a quantitative thermodynamic expression for solute segregation, which is given for a ternary alloy by [54]:

$$\Gamma_{\mathrm{Si}}^{rel} = \Gamma_{\mathrm{Si}} - \Gamma_{\mathrm{Cu}} \frac{c_{\mathrm{Al}}^{\alpha} c_{\mathrm{Si}}^{\theta'} - c_{\mathrm{Al}}^{\theta'} C_{\mathrm{Si}}^{\alpha}}{c_{\mathrm{Al}}^{\alpha} c_{\mathrm{Cu}}^{\theta'} - c_{\mathrm{Al}}^{\theta'} c_{\mathrm{Cu}}^{\alpha}} - \Gamma_{\mathrm{Al}} \frac{c_{\mathrm{Si}}^{\alpha} c_{\mathrm{Cu}}^{\theta'} - c_{\mathrm{Si}}^{\theta'} c_{\mathrm{Cu}}^{\alpha}}{c_{\mathrm{Al}}^{\alpha} c_{\mathrm{Cu}}^{\theta'} - c_{\mathrm{Al}}^{\theta'} c_{\mathrm{Cu}}^{\alpha}} \quad (1)$$

where $\Gamma_{\mathrm{Si}}^{rel}$ is the Gibbsian interfacial excess of Si relative to Cu and Al; Γ_{Si}, Γ_{Cu} and Γ_{Al} are the Gibbsian interfacial excesses of Si, Cu and Al, respectively; and c_i^{α} and $c_i^{\theta'}$ are the concentrations of an element i (i = Al, Cu or Si) in the α-Al matrix and θ' platelets. In Fig. 12, Al and Cu exhibit delocalized interfacial excesses, as opposed to the localized interfacial excess of Si. The shaded areas in the proxigram represent the individual Γ_is. The values of Γ_i are determined using proxigram concentration profiles from

$$\Gamma_i = \rho \Delta x \sum_{m=1}^{p} \left(c_i^m - c_i^k \right) \quad (2)$$

where ρ is the atomic density, Δx is the distance between the p concentration data points in the proxigram, c_i^k is the concentration of an element i at each data point [55], and $k = \alpha$ on the α-Al matrix side and $k = \theta'$ on the precipitate side of the heterophase interface. (The theoretical atomic density of a θ' precipitate is 63.38 atoms nm^{-3}, based on its unit cell dimensions [6], which is close to that of Al.) A similar method was used for determining interfacial excesses for 1-D concentration profiles across grain-boundaries in a binary alloy [56,57]. Marquis et al. [19,58,59] and Isheim et al. [60] employed this method for quantitative analyses of interfacial segregation of solute atoms across heterophase interfaces. The Gibbs dividing surface that is placed at the inflection point of the Al concentration profile coincides with the origin of the proxigram. The relative Gibbsian interfacial excess concentration does not depend on the location of the Gibbs dividing surface [54,61–63]. The relative Gibbsian interfacial excess of Si with respect to Al and Cu (Eq. (1)), is

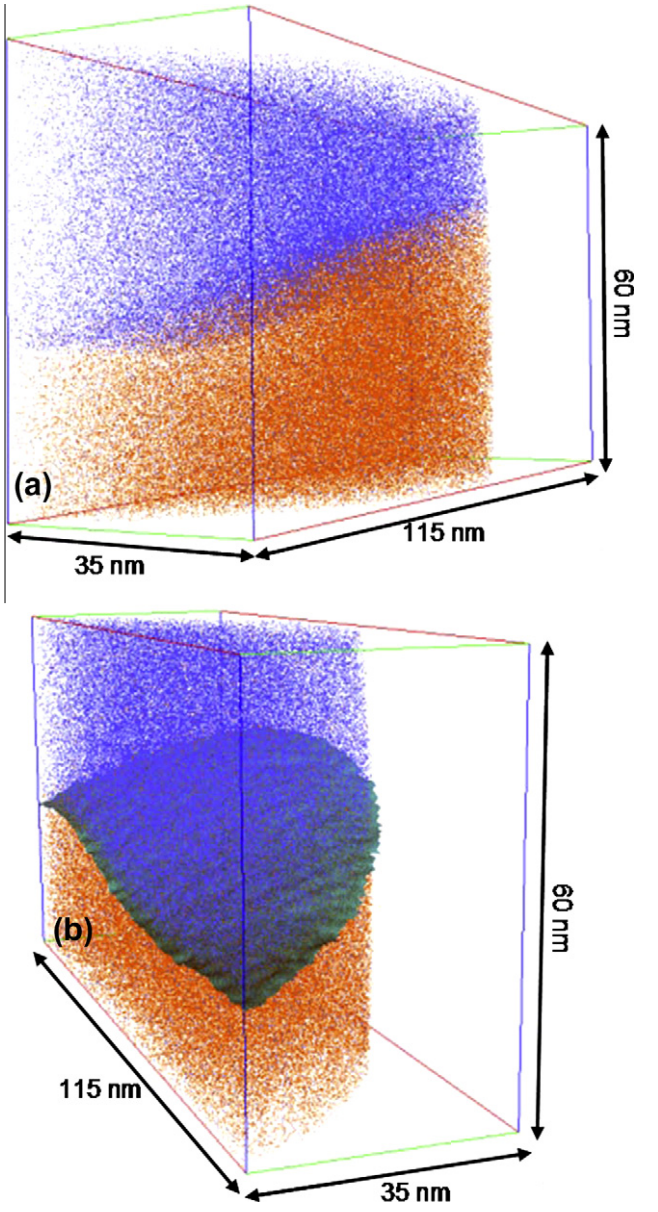

Fig. 11. (a) θ' precipitate from a sample of alloy B aged at 533 K for 4 h that is perpendicular to the analysis direction; green laser pulsing is used. (b) Isoconcentration surface created with respect to 9 at.% Cu; this surface delineates the coherent interface with the α-Al matrix.

0.39 ± 0.078 atom nm^{-2}. A summary of the relevant quantities used in this analysis are given in Table 3.

3.3.5. First-principles calculations

To explain the observed partitioning of Si solute atoms in the Si-containing B alloys, we performed a series of first-principles calculations (at 0 K) of bulk point-defect and solute-solution energies, as well as interfacial solute-segregation energies. This methodology has previously been used to examine solute energetics in several other systems [64–69]. We begin by discussing the interfacial segregation calculations.

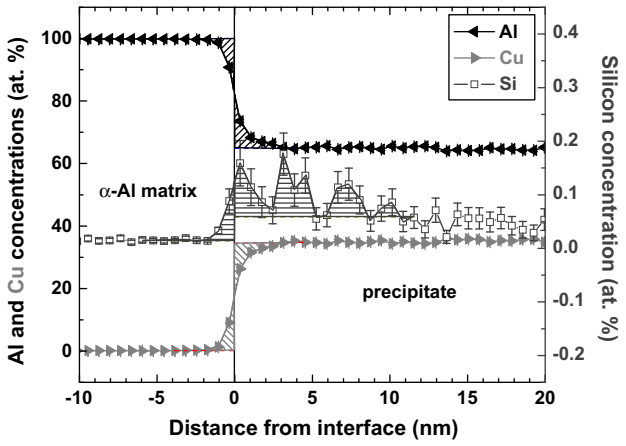

Fig. 12. Proxigram from a sample of alloy B aged at 533 K for 4 h. The shaded area indicates interfacial segregation. Green laser pulsing is used.

3.3.6. Interfacial segregation calculations

The segregation energy, ΔE_{seg}, is defined as the difference in the respective heats of solution, ΔE_{sol}, for insertion of a Si solute atom at a site near the matrix/precipitate interface, ΔE_{sol} (int), vs. insertion at a bulk-like site in the Al matrix, ΔE_{sol} (bulk):

$$\Delta E_{seg} = \Delta E_{sol}(\text{int}) - \Delta E_{sol}(\text{bulk}) \tag{3}$$

Given the similar atomic radii of Al, Cu and Si, we assume that Si occurs only as a substitutional solute atom. For segregation at an Al site, the expression for ΔE_{seg} simplifies to the difference in total energy for a supercell having a solute atom in the matrix (within the "bulk" or center layer of the Al slab, Al_b plane in Fig. 1), and another with a solute atom substituting for an Al atom in a plane other than the bulk Al plane. Taking the example of Si segregation at the Al_i layer (the layer in the Al slab immediately adjacent to the interface), this energy is expressed as:

$$\Delta E_{seg} = E(\text{Si} \rightarrow \text{Al}_i) - E(\text{Si} \rightarrow \text{Al}_b) \tag{4}$$

Eq. (4) applies whether the Al segregation site resides in the Al matrix (Al_i, Al_{i-1}, etc.) or at an Al sublattice site in θ' (i.e. $\theta_i'^{Al}$, $\theta_{i-1}'^{Al}$). We adopt a sign convention such that sites having $\Delta E_{seg} < 0$ are energetically favorable for solute segregation.

In addition to segregation at Al sites, we also considered segregation at Cu sites within θ'. For this scenario a slightly modified form of Eq. (4) is required. Assuming, for example, that segregation occurs at the coherent $\theta_i'^{Cu}$ layer, then:

$$\Delta E_{sol}(\text{int}) = E(\text{Si} \rightarrow \theta_i'^{\text{Cu}}) - (E_0 - \mu_{\text{Cu}} + \mu_{\text{Si}}) \tag{5}$$

and

$$\Delta E_{sol}(\text{bulk}) = E(\text{Si} \rightarrow \text{Al}_{\text{bulk}}) - (E_0 - \mu_{\text{Al}} + \mu_{\text{Si}}) \tag{6}$$

where E_0 refers to the energy of the interface supercell in the absence of solutes, and μ_n are the chemical potentials of n = Cu, Si or Al. Substituting Eqs. (5) and (6) into Eq. (3) yields:

$$\Delta E_{seg} = E(\text{Si} \rightarrow \theta_i'^{\text{Cu}}) - E(\text{Si} \rightarrow \text{Al}_{\text{bulk}}) + \mu_{\text{Cu}} - \mu_{\text{Al}} \tag{7}$$

which requires an evaluation of the chemical potentials of Cu and Al atoms. If local thermodynamic equilibrium is established, these quantities may be extracted using the following two thermodynamic relations [70,71]:

$$\mu_{\text{Al}}(\text{matrix}) = \mu_{\text{Al}}(\theta') \equiv \mu_{\text{Al}} \tag{8}$$

and

$$2\mu_{\text{Al}}(\theta') + \mu_{\text{Cu}}(\theta') = E(\theta') \tag{9}$$

Here $E(\theta')$ is the energy per formula unit of bulk θ'. That is, the chemical potential for Al must be the same in both the Al matrix (μ_{Al}(matrix)) and in θ' phase ($\mu_{\text{Al}}(\theta')$), otherwise the system could lower its energy by transferring Al atoms from one phase to the other, in violation of our assumption of local equilibrium. Since μ_{Al} and $E(\theta')$ can be determined from calculations on bulk-like slabs of Al and θ', sufficient information exists to solve for $\mu_{\text{Cu}}(\theta')$, and calculate ΔE_{seg}.

Using the above equations, Fig. 13 displays the calculated segregation energy of a Si solute atom as a function of distance from the coherent Al/θ' interface. Two segregation energies are reported for each layer: for layers containing Al atoms (Al_x and $\theta_x'^{Al}$) these energies correspond to the two symmetry-distinct segregation sites. Consistent with the proxigram data in Figs. 10 and 12, our calculations demonstrate that there is no significant energetic driving force for Si segregation at sites on the matrix side of the interface (Al_i, Al_{i-1}, Al_{i-2}), as $\Delta E_{seg} \sim 0$ here. Similarly, there is no significant attraction expected to Al sites within θ' (i.e. at the $\theta_i'^{Al}$ and θ_{i-1}^{Al} layers). Alternatively, Si segregation at the Cu sites in θ' is predicted to be strongly favorable, with large ΔE_{seg}s of -0.2 to -0.3 eV atom^{-1}, suggesting that elevated Si concentrations on the θ' side of the interface is thermodynamically reasonable.

Silicon ΔE_{seg}s for the semi-coherent interface are plotted in Fig. 14. Due to the lower symmetry of this interface, each atomic layer parallel to the interface contains four geometrically distinct sites. We studied segregation at each of these sites, and thus report four ΔE_{seg}s per plane. Unlike

Table 3
Details of the interfacial segregation analysis after aging at 533 K for 4 h.

	α-Al matrix (at.%)	θ′-precipitate (at.%)	Confined interfacial excess (atoms/nm^2)	Relative confined interfacial excess (atoms/nm^2)
Al	99.88 ± 0.016	65.005 ± 1.2	–	–
Cu	0.106 ± 0.016	34.94 ± 1.2	–	–
Si	0.014 ± 0.008	0.0527 ± 0.015	0.38 ± 0.078	0.39 ± 0.078

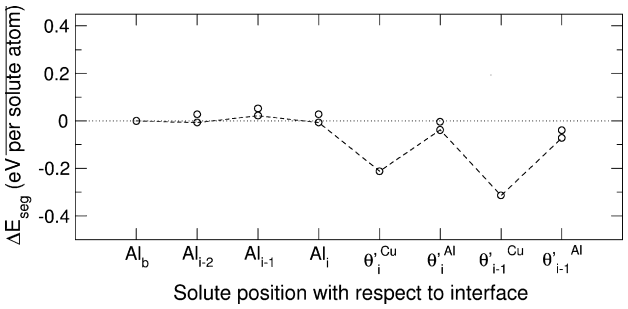

Fig. 13. Calculated Si segregation energies as a function of solute position relative to the coherent Al/θ' interface. The nomenclature for solute positions is as described in Fig. 1. Two segregation energies are reported for each layer: for layers containing Al atoms (Al_x and θ'^{Al}_x), these energies correspond to the two symmetry-distinct segregation sites; for Cu-containing layers θ'^{Cu}_x, the energies reflect the two possible choices of μ_{Cu}, as described in the text. The most favorable sites for segregation within a given plane are indicated using a dashed line.

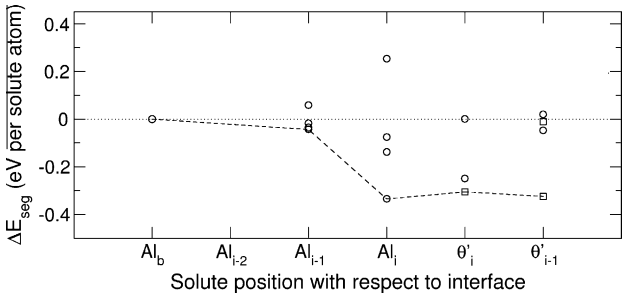

Fig. 14. Calculated Si segregation energies as a function of solute position relative to the semi-coherent Al/θ' interface. Circles (squares) represent segregation to Al (Cu) sites. Multiple segregation energies are listed for each interfacial plane, reflecting the presence of several distinct sites per plane. The most favorable sites for segregation within a given plane are indicated using a dashed line.

what was found for the coherent system, Si segregation at the semi-coherent interface is expected to occur on both sides of the interface: our calculations predict the existence of two sites within the Al_i plane with $\Delta E_{seg} < -0.1$ eV atom^{-1}. One of these sites is highly attractive for Si, having $\Delta E_{seg} = -0.33$ eV atom^{-1}. This site is positioned such that it continues the crystal structure of the θ' Cu sublattice into the Al matrix. It may therefore be chemically similar to a Cu site in θ'. As discussed above, Cu sites are attractive for Si segregation at the coherent interface. Indeed this site's ΔE_{seg} is similar to what we calculated for Cu sites in θ' at both interfaces.

On the θ' side of the semi-coherent interface, Cu sites also provide highly attractive segregation sites ($\Delta E_{seg} < -0.3$ eV atom^{-1}), similar to the coherent system. However, unlike the coherent interface, where no Al sites in θ' are favorable for Si occupation, one Al sublattice site in θ' is strongly attractive for Si ($\Delta E_{seg} = -0.25$ eV atom^{-1}). It is notable that this site is located within the θ'_i layer, which is immediately adjacent to the interface. Deeper into θ' (at the θ'_{i-1} layer) Si segregation to Al sublattice sites is predicted to be negligible, consistent with calculated ΔE_{seg}s to Al sites in the coherent system, suggesting that it is not energetically preferable for Si to occupy bulk-like sites within the Al sublattice of θ'. That is, segregation of Si at θ' Al sublattice sites is limited to sites that are immediately adjacent to the interface.

3.3.7. Bulk point defect and solute–solution calculations

As described, one of the key findings of our LEAP tomographic experiments is the Cu deficiency of the GPII and θ' precipitates observed at 438 and 463 K. This deficiency may be caused by limited Cu diffusion at the aging temperatures: see Section 4.2 below. Another possibility, which we explore using first-principles calculations, relates to the energetics of vacancies and anti-site defects in the θ' phase. Regarding vacancies, the top panel of Fig. 15 displays the energy of formation of a vacancy at 0 K on either the Cu or Al sublattice-sites of θ'. The vacancy formation energy on the Cu sublattice, 0.88 eV, is 0.95 eV smaller than on the Al sublattice sites, 1.83 eV, suggesting that vacancies may lower the Cu concentration in θ'. Similarly, the bottom panel of Fig. 15 reveals that 0.74 eV less energy is required to form an Al anti-site defect, 0.55 eV, on the θ' Cu sublattice (denoted "Al_{Cu}", corresponding to an Al-rich/Cu-deficient defect) than to substitute a Cu atom on an Al sublattice site (Cu_{Al}, 1.29 eV). While these energetics are qualitatively consistent with the measured Cu deficiency in θ', the magnitude of the calculated formation energies suggests that the resulting point defect concentrations are too small to alter the stoichiometry of the precipitate significantly. For example, at 463 K the concentration of Cu vacancies is $N_v^{Cu} \sim 10^{-10}$ atomic fraction, while the concentration of Al_{Cu} defects is $\sim 10^{-6}$ atomic fraction. These values are four to eight orders of magnitude smaller than what is needed to account for the experimental data, and therefore we conclude that these defects do not play a significant role in accounting for the Cu deficiency of θ'.

A second key observation of our LEAP tomographic experiments is the partitioning of Si atoms to θ' precipitates in alloys containing ~200 at. ppm Si. Here we examine the extent to which this behavior can be attributed to bulk thermodynamics by computing the relative heats of

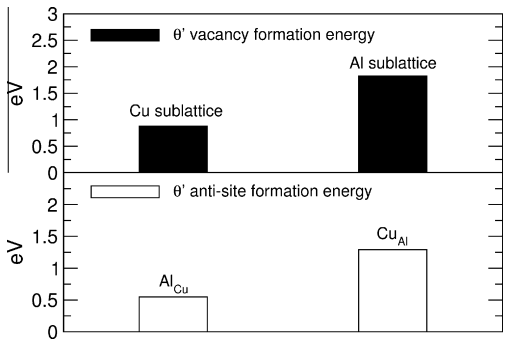

Fig. 15. Calculated formation energies for vacancies (top) and anti-site defects (bottom) in bulk θ' as a function of sublattice location. "Al_{Cu}" refers to the anti-site formation energy of an Al atom on a Cu sublattice site.

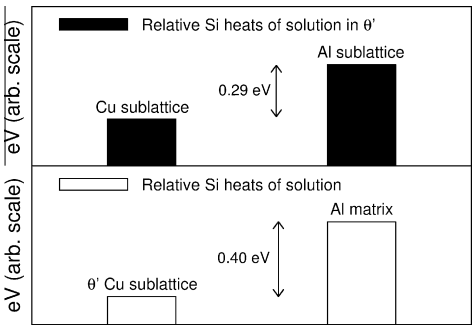

Fig. 16. Top: calculated relative heats of solution for Si insertion into θ' as a function of sublattice site. Bottom: comparison of the calculated relative heats of solution for Si insertion into bulk Al and a Cu sublattice site in θ'.

solution for Si insertion into the bulk Al matrix vs. into θ' precipitates at 0 K. The top panel in Fig. 16 demonstrates that, of the two sublattices in the θ' phase, the Cu sublattice sites are the most energetically favorable by 0.29 eV atom^{-1} for Si substitution. This behavior is consistent with our interfacial segregation calculations, where the most favorable sites for Si segregation in θ' are Cu sublattice sites. The bottom panel, Fig. 16, compares Si substitution into these Cu sublattice sites with substitution into bulk Al. As shown, Si occupation of the θ' Cu sublattice sites is strongly preferred, by 0.40 eV atom^{-1}, over Al matrix sites. We conclude that the observed partitioning of Si to the θ' phase can be at least partially attributed to the bulk thermodynamics of the θ' phase.

4. Discussion

4.1. 3-D LEAP tomographic analyses of GPII zones

The 438 K for 8 h aging treatment produces thin platelet-like precipitates that are identified as GPII platelets; no θ' platelets are observed for this case. Prior XRD studies of aging at this temperature, by Hardy [12,13] and Silcock et al. [14], are in general agreement with this result. In addition to a majority GPII phase, Silcock et al. [14] detected about 20 vol.% θ' precipitates after aging an Al–4 wt.% Cu alloy for 3.5 days. Boyd and Nicholson [17] used TEM for their 438 K aging studies of a similar alloy and observed that the GPII zones commenced transforming to θ' precipitates only when the aging time was >48 h.

Our LEAP tomographic compositional analyses of these GPII zones (Fig. 6b) exhibit Cu concentrations of 10–40 at.% and therefore do not agree with the expected GPII stoichiometry, Al_3Cu [3]. Likewise, other atom-probe experiments do not detect a 100% pure Cu layer in either the GPI or GPII zones [23], as anticipated by extant structural models. To the best of our knowledge, the study by Hono et al. [21] represents the only attempt at a compositional analysis of GPII zones by APT. They reported 40–50 at.% Cu in GPII zones in their study of an Al–1.7 at.% Cu alloy aged at 383 K for 133.3 h. Even though the atom probe tomograph offers the highest spatial resolution among all the available analytical techniques, resolution of an individual atomic layer of Cu in GP zones is still difficult. This difficulty is, in part, due to the fact that an atomic plane from the sample is no longer an atomistically flat plane after field evaporation and reconstruction. In addition, the composition of a GP zone is not entirely well defined, due to the ambiguity associated with how many Al atomic layers surrounding the Cu-rich layers should be considered as part of the zone. As the thickness of the zones gets smaller, this ambiguity will lead to larger uncertainty in the composition of the zone. For both of the reasons above, the APT measurements of the composition and thickness of the GPII zones should be considered with some caution.

4.2. 3-D LEAP tomographic analyses of θ'platelets: 463 K and 533 K

LEAP tomography of specimens aged at 463 K for 8 h exhibits θ' precipitates with an aspect ratio (diameter/thickness) >20. Our thickness value, 7.95 ± 1.47 nm, is consistent with the results of Silcock et al. [14], but our compositional analyses exhibit a range of Cu core concentrations of ~20–35 at.% (Fig. 7d), which deviate from the stoichiometric value of 33.3 at.%. It should be noted that θ' precipitates are thicker than GP zones, and thus the errors in composition due to thickness quoted above should be smaller for θ' precipitates than for GP zones. Further, we do not find a correlation between the thickness of a θ' precipitate and its Cu concentration in the 463 K aged specimens, which suggests that the measured Cu deficiency of these precipitates is not merely due to the effects of thickness. A difference in the evaporation fields of the α-Al matrix and the θ' platelets may explain this discrepancy [58]. However, the facts that (i) there exists some θ' precipitates (~10% of the total; Fig. 7d) with near-stoichiometric Cu core concentrations and (ii) the samples aged at 533 K for 4 h exhibit θ' Cu core concentrations close to the stoichiometric value suggest that field-evaporation artifacts cannot explain the Cu deficiency.

Kinetic limitations during precipitate growth, perhaps due to a small diffusivity of Cu in Al, may result in Cu-deficient precipitates. The root-mean-square (RMS) diffusion distance of Cu in Al is $\sqrt{4Dt}$, where $D = 2.89 \times 10^{-20}$ m^2 s^{-1} is the tracer diffusivity of Cu in Al at 463 K [72] and t is the aging time; the RMS diffusion distance for $t = 8$ h is 57.7 nm. This distance is very similar to the average center-to-center spacing between θ' precipitates, 57.3 nm. Since the relevant diffusion distance is the precipitate edge-to-edge spacing, and this distance is smaller than the center-to-center spacing, it is unlikely that the rate of Cu diffusion in Al can account for the Cu deficiency of the θ' precipitates.

The off-stoichiometry of the θ' precipitates aged at 463 K raises the question of the site occupancy of the excess Al atoms in the platelets. We are not aware of any articles addressing whether anti-site defects or Cu vacancies are

energetically favorable in the θ' phase. Furthermore, no information is available regarding the ability of θ' precipitates to dissolve Al or Cu. Our first-principles calculations address these issues directly. They indicate that the Cu sublattice sites are the most energetically favorable sites for vacancy formation in θ', and that the formation of Al anti-sites on the Cu sublattice (Al_{Cu}) is more favorable than the formation of point defects of the opposite sense (Cu_{Al}). Although these point-defect types would appear to favor a Cu-deficient/Al-rich θ' stoichiometry, their large formation energies suggest that they do not have a significant impact on the stoichiometry. Solubility data for Si in θ' is also unavailable. Based on our first-principles solute-solution calculations, we expect that in Si-containing alloys the Si atoms strongly prefer Cu sublattice sites in θ' precipitates over Al sites in either the Al matrix or the θ' precipitates. Thus, Si will compete with Cu to occupy Cu sublattice sites in θ', thereby contributing to the observed Cu deficiency of θ' in Si-containing alloys.

Although Si is one of the main elements in commercial θ'-precipitation-strengthened Al–Cu alloys [30,73,74], there are few studies on the role of Si in the precipitation behavior of the θ' phase in Al–Cu alloys. Mitlin et al. [75] investigated the effect of Si on an Al–0.86Cu–0.97Si at.% alloy and proposed that Si had a catalytic effect on the precipitation of θ' precipitates. In support of this hypothesis, they provided TEM and electron diffraction evidence for a highly irregular precipitate morphology: θ' precipitates containing Si platelets. However, no chemical analyses of these structures were performed. We observe a similar catalytic effect of Si on GPII platelets at 438 K and 8 h aging, where the N_v value of GPII platelets is a factor of three greater for the Si-containing alloy compared to the Si-free one. This effect on the precipitation of θ' platelets could not, however, be directly verified by the current LEAP tomographic analyses because of the difficulty associated with capturing statistically significant numbers of large diameter ($\geqslant$180 nm) θ' platelets.

In addition to reporting evidence of Si atoms in GPII zones and θ' precipitates, our observation of segregation of Si at the α-Al/θ' coherent interface is another new and significant finding. Table 4 summarizes the change in Si concentration within the α-Al matrix, at the matrix/precipitate interface and at the θ' core for samples aged at 463 vs. 533 K. Additionally, Table 4 displays data for $K_{si}^{\theta'/\alpha\text{-Al}}$: this ratio is 3.8 for the sample aged at 533 K, which is a factor of two less than the value obtained for aging at 463 K (7.4). The smaller value of $K_{si}^{\theta'/\alpha\text{-Al}l}$ at 533 K is due to a reduction in the Si concentration in the θ' platelet core ($c_{Si}^{\theta'}$) compared to aging at 463 K. While the Si core concentration decreases upon increasing aging temperature, the Si concentration at the coherent heterophase interface responds in the opposite sense, increasing by nearly a factor of six with increasing aging temperature. Assuming that the entropy of segregation is small, the latter is indicative of a nonequilibrium kinetic effect, as an attractive enthalpic interaction with an interface implies that the Gibbsian excess of a solute must decrease with increasing temperature.

Combining the above observations, one possible explanation for the behavior of Si in these alloys is as follows: Si catalyzes the nucleation of the GPII zones as manifested by a threefold increase in the N_v value in the Si-containing alloy B. On further aging [76], θ' platelets evolve by reprecipitation, preceded by dissolution of GPII zones. TEM studies [77] have confirmed the heterogeneous nucleation of θ' precipitates on GPII zones with some assistance from dislocations [76]. The fact that both the GPII zones after a 438 K aging treatment, and the θ' platelets on aging at 463 K exhibit similar Si core concentrations lends further credibility to this explanation. Moreover, first-principles calculations for Si partitioning demonstrates that Si is strongly attracted to θ' platelets. Consequently, Si most likely catalyzes the nucleation of θ' platelets. The additional thermodynamic driving force provided by stabilizing the formation of θ' precipitates has the effect of decreasing the net reversible work for forming a critical size nucleus [78]. In addition to this bulk thermodynamic effect, segregation of Si at the matrix/precipitate interface may also impact the kinetics of precipitate nucleation. In particular, Si may lower the interfacial free energy (γ) by migrating to the interface. Since the nucleation current is influenced strongly by γ, any reduction in γ will increase the θ' nucleation rate.

4.3. Reduction in interfacial free energy due to segregation of Si

From the Gibbs adsorption isotherm for a system with two phases and $n \geqslant 3$ components [79], a coefficient for the reduction of γ at a concentration c_i due to segregation of component i at the heterophase interface, assuming a dilute solution model, is given by [19,56,58,60,80–82]:

$$\left.\frac{\partial\gamma}{\partial c_i}\right|_{T,p,\mu_3,\ldots,\mu_{i-1},\mu_{i+1},\ldots,\mu_n} = -k_B T \frac{\Gamma_i^{rel}}{c_i} \tag{10}$$

where Henry's law for dilute solutions is assumed, μ_i is the chemical potential of component i, k_B is Boltzmann's con-

Table 4
Evolution of Si concentration with aging temperature in the α-Al matrix and θ' precipitate core, and at the matrix/precipitate interface.

	Si in the α-Al matrix (at.%)	Si at the θ'-precipitate core (at.%)	Si partitioning ratio $K_{Si}^{\theta'/\alpha\text{-Al}} = \frac{c_{Si}^{\theta'}}{c_{Si}^{\alpha\text{-Al}}}$	Si concentration at the interface (at.%)
463 K–8 h	0.0129 ± 0.003	0.096 ± 0.009	7.4	0.0272 ± 0.004
533 K–4 h	0.0140 ± 0.008	0.0527 ± 0.015	3.8	0.1588 ± 0.042

stant and T is the absolute temperature. At 533 K, the relative Gibbsian interfacial excess of Si is 0.39 ± 0.08 atoms nm^{-2} (Fig. 12). The total reduction of γ due to the interfacial solute excess is calculated by evaluating the following integral [83,84]:

$$-\frac{1}{k_B T \cdot \Gamma_i^{\mathrm{rel}}} \int_{\gamma_{\mathrm{initial}}}^{\gamma_{\mathrm{final}}} d\gamma = \int_{c_i^{\mathrm{initial}}}^{c_i^{\mathrm{final}}} \frac{dc_i}{c_i} \tag{11}$$

which yields a value of -7.0 mJ m^{-2}. Here c_i^{initial} and c_i^{final} are the Si concentration of the α-Al matrix and the peak concentration of Si at the α-Al/θ' interface, respectively (Table 4).

Similar solute segregation effects at a coherent heterophase interface between precipitates and the α-Al matrix have been reported for Al–Sc–Mg. Marquis et al. [19,58] observed magnesium segregation at the coherent α-Al/Al_3Sc interface, where the reduction of interfacial free energy is -15 mJ m^{-2} and the driving force for segregation is mainly electronic (chemical) in origin. Recently, qualitative evidence of Cu segregation at the α-Al/Q′ interface was obtained with energy-filtered TEM for the Al–Mg–Si–Cu system [85]. The Q′ phase is a metastable quaternary Al–Mg–Si–Cu phase with a hexagonal crystal structure, which occurs as rod-shaped precipitates: there are conflicting reports concerning its stoichiometric composition [86–89]. LEAP tomography is an appropriate instrument to obtain quantitative chemical information from precipitates and their heterophase interfaces at the subnanometer scale. Our current study demonstrates that Si segregation is measureable when the total Si concentration is only ~200 at. ppm.

5. Conclusions

A combination of experimental and computational techniques (XRD, TEM, APT and first-principles calculations) are employed to study precipitation in a series of Al–4 wt.% Cu (Al–1.74 at.% Cu) alloys aged under varying conditions and containing 200–300 at. ppm Fe and Si impurities. The primary phenomena investigated are: (i) compositional evolution of GPII zones and θ' precipitates; and (ii) solute segregation behavior at α-Al/θ' interfaces. The major results of this study include:

1. The large diameter and small number density of θ' precipitates (~180 nm and $\sim 1.5 \times 10^{21}$ m^{-3}, respectively, after aging for 8 h at 463 K) make the 3-D LEAP tomographic analyses challenging. The use of a wide field-of-view detector and laser pulsing, however, permits the collection of large datasets from which statistically significant conclusions regarding precipitate composition are drawn.
2. In contrast to the expected equilibrium composition of Al_3Cu, GPII zones (~2 nm thick, ~22 nm diameter) with a wide compositional range of 10–40 at.% Cu are obtained for aging at 438 K. At higher aging temperatures (463 and 533 K) only θ' precipitates are observed. Increasing the aging temperature from 463 to 533 K leads to a thickening of the θ' precipitates from ~8 to ~50 nm, and an order-of-magnitude decrease in number density: from 1.5×10^{21} to 1.5×10^{20} m^{-3}.
3. After aging at 463 K for 8 h, the θ' precipitates exhibit a range of Cu-deficient core concentrations of ~20–35 at.%, which differ from the equilibrium composition of Al_2Cu. Limited Cu diffusion and/or the formation of point defects (Cu vacancies and anti-site defects) were ruled out as possible mechanisms leading to this Cu deficiency. In contrast, alloys aged at 533 K for 4 h exhibited precipitates with Cu core concentrations close to the equilibrium value. The cause of the Cu deficiency in the θ' precipitates at the lower aging temperatures remains an open issue.
4. We observe evidence of partitioning of Si to the GPII zones and θ' precipitates in the Al–Cu system. Additionally, significant Si segregation is observed at the coherent α-Al/θ' interface, with aging at 533 K resulting in an interfacial Si concentration >11 times that in the α-Al matrix and a reduction of the interfacial free energy by ~7 mJ m^{-2}. These effects are detected even though the bulk concentration is only ~200 at. ppm Si. In agreement with these experimental results, first-principles calculations predict a strong thermodynamic driving force favoring Si atom partitioning to Cu sublattice sites in θ' precipitates.
5. On the basis of (i) the larger number density of GPII zones for Si-containing alloys, (ii) the observation of Si segregation at α-Al/θ' interfaces and (iii) the calculated thermodynamics of Si partitioning to θ', we conclude that Si catalyzes the heterogeneous nucleation of GPII zones and θ' precipitates.

Acknowledgements

A.B. and D.N.S. acknowledge financial support from the Ford-Boeing-Northwestern Alliance. Atom-probe tomographic measurements were performed at the Northwestern University Center for Atom-probe Tomography (NUCAPT). Support for the purchase of the LEAP Tomograph was provided by NSF-MRI (DMR 0420532) and ONR-DURIP (N00014-0400798 and N00014-0610539). Synchrotron experiments were performed using the DuPont–Northwestern–Dow beam line at the Advanced Photon Source, Argonne National Laboratory. We thank Drs. Denis Keane and Dieter Isheim for their assistance with the synchrotron and atom-probe tomography experiments, respectively. We also thanks Drs. D.S. Shih and K.K. Sankaran (Boeing), and M. Li and J. Allison (Ford Motor Company) for their continuous interest, support and helpful comments. C.W. acknowledges the US Automotive Materials Partnership Project on ICME for Magnesium. This material is based upon work supported by the Department of Energy National Energy

Technology Laboratory under Award Number Nos. DE-FC05-95OR22363, DE-FC05-02OR22910, and DE-FC26-02OR22910.

Appendix A

A.1. Bin size analysis in 3-D atom-probe tomography

A crucial parameter for quantitative analyses, employing 3-D atom-probe tomography, of heterophase interfacial segregation is the choice of the correct bin size. The bin size was varied from 0.1 to 3 nm to determine the most appropriate value in terms of good statistics and an acceptable error of ±10%. Fig. A1 demonstrates the effect of the variation of bin size on the Si concentration profiles. A larger bin size ensures better statistics and a smaller standard deviation, while concomitantly reducing the spatial resolution. Table A1 demonstrates how the sample count changes with bin size. Fig. A2 displays the variation of the α-Al matrix and θ' core compositions and the area under the Si concentration profile with bin size. The area under the Si concentration profile graphically represents solute segregation at the heterophase interface (Fig. 15). The average composition of the α-Al matrix as well as the core composition of the θ' precipitates achieves a plateau at a bin size of 0.5 nm. Simultaneously, the area under the Si concentration profile ceases to vary, which is indicative of the desired numerical stability of the analysis. Based on these results, a bin size of 0.7 nm was chosen for the calculation of the relative Gibbsian interfacial excess concentration of Si with respect to Al and Cu.

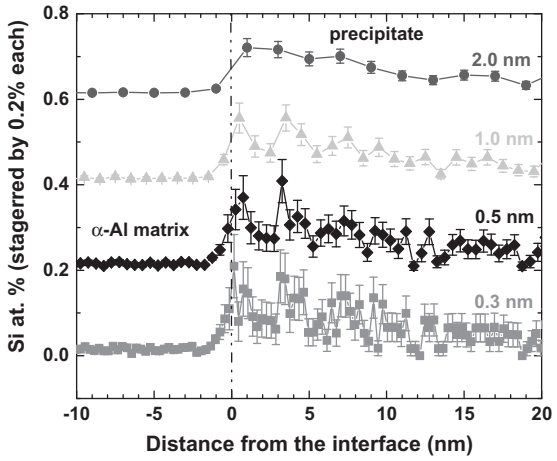

Fig. A1. Effect of bin size on the Si concentration profile for the sample aged at 533 K for 4 h. Green laser (wavelength = 532 nm) pulsing is used.

Table A1
Effect of bin size on the sample count.

Bin (nm)	0.1	0.3	0.5	0.7	0.9	1.0
Sample count	1.3 k	4.0 k	6.5 k	9 k	11 k	12 k

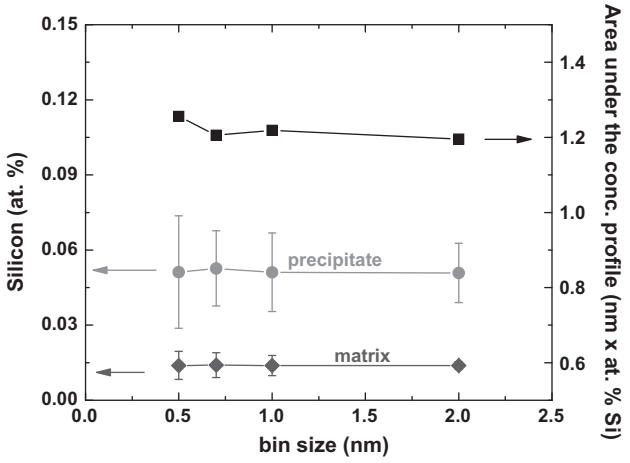

Fig. A2. Effect of bin size on the average and the area under the silicon concentrations (at.%) profile.

References

[1] Gayle FW, Goodway M. Science 1994;266:1015.
[2] Konno TJ, Hiraga K, Kawasaki M. Scr Mater 2001;44:2303.
[3] Gerold V. Scr Metall 1988;22:927.
[4] Wolverton C. Phil Mag Lett 1999;79:1362.
[5] Wolerton C, Ozolins V. Phy Rev Lett 2001;86:5518–21.
[6] Silcock JM. Acta Cryst 1956;9:680.
[7] Laird C, Aaronson HI. Trans Metall Soc AIME 1968;242:1393.
[8] Aaronson HI, Laird C. Ford Motor Co. Scientific laboratory report no. SL 67-52; 1967.
[9] Aaronson HI, Clark JB, Laird C. Met Sci J 1968;2:155.
[10] Vaithyanathan V, Wolverton C, Chen LQ. Phy Rev Lett 2002;88:125503-1.
[11] Vaithyanathan V, Wolverton C, Chen LQ. Acta Mater 2004;52:2973.
[12] Hardy HK. J Inst Met 1951;79:321.
[13] Hardy HK. J Inst Met 1953–1954;82:236.
[14] Silcock JM, Heal TJ, Hardy HK. J Inst Met 1953–1954;82:239.
[15] Weatherly GC, Nicholson RB. Phil Mag 1968;17:801.
[16] Dahmen U, Westmacott KH. Phys Stat Sol 1983;80(a):249.
[17] Boyd JD, Nicholson RB. Acta Metall 1971;19:1379.
[18] Biswas A, Siegel DJ, Seidman DN. Phys Rev Lett 2010;105:076102-1.
[19] Marquis EA, Seidman DN, Asta M, Woodward C, Ozolins V. Phys Rev Lett 2003;91:036101-1.
[20] Mao Z, Sudbrack CK, Yoon KE, Martin G, Seidman DN. Nat Mater 2007;6:210.
[21] Hono K, Sakurai T, Pickering HW. Met Trans A 1989;20A:1585.
[22] Bigot A, Danoix F, Auger P, Blavette D, Menand A. Appl Surf Sci 1996;94/95:261.
[23] Karlik M, Bigot A, Jouffrey B, Auger P, Belliot S. Ultramicro 2004;98:219.
[24] Shollock BA, Grovenor CRM, Knowlcs KM. Scr Met Mater 1990;24:1239.
[25] Sano N, Hono K, Sakurai T, Hirano K. Scr Met Mat 1991;25:491.
[26] Ringer SP, Hono K, Sakurai T. Appl Surf Sci 1995;87/88:223.
[27] Honma T, Saxey DW, Ringer SP. Mater Sci For 2006;519–521:203.
[28] Choi PP, Al-Kassab T, Kirchheim R. Scr Mater 2005;53:323.
[29] Srivastava C, Thompson GB, Reinhard D, Sebastian J, Prosa TJ, Larson DJ, et al. Microsc Microana 2006;12(Suppl. 2):1752.
[30] Weakley-Bolin SC, Donlon W, Wolverton C, Jones JW, Allison JE. Met Mater Trans A 2004;35A:2407.
[31] Krakauer BW, Hu JG, Kuo SM, Mallick RL, Seki A, Seidman DN, et al. Rev Sci Instrum 1990;61:3390.
[32] Krakauer BW, Seidman DN. Rev Sci Instrum 1992;63:4071.
[33] Seidman DN, Stiller K. Mater Res Soc Bull 2009;34(10):717–21.
[34] Seidman DN, Stiller K. Mater Res Soc Bull 2009;34(10):717–49.

[35] Bajikar SS, Larson DJ, Kelly TF, Camus PP. Ultramicroscopy 1996;65:119.
[36] Kelly TF, Camus PP, Larson DJ, Holzman LM, Bajikar SS. Ultramicroscopy 1996;62:29.
[37] Kelly TF, Larson DJ. Mater Charact 2000;44:59.
[38] Seidman DN. Annu Rev Mater Res 2007;37:127.
[39] Seidman DN. Rev Sci Instrum 2007;78:031101-1.
[40] Kelly TF, Miller MK. Rev Sci Instrum 2007;78:031101.
[41] Hellman OC, Blatz du Rivage J, Seidman DN. Ultramicroscopy 2003;95:199.
[42] Hellman OC, Vandenbroucke JA, Rüsing J, Isheim D, Seidman DN. Microsc Microanal 2000;6:437.
[43] Booth-Morrison C, Weninger J, Sudbrack CK, Mao Z, Noebe RD, Seidman DN. Acta Mater 2008;56:3422.
[44] Siegel DJ, Hamilton JC. Acta Mater 2005;53:87.
[45] Perdew JP et al. Phys Rev B 1992;46:6671.
[46] Hohenberg P, Kohn W. Phys Rev 1964;136:B864.
[47] Kohn W, Sham LJ. Phys Rev 1965;140:A1133.
[48] Kresse G, Furthmüller. J Phys Rev B 1996;54:11169.
[49] Blöchl PE. Phys Rev B 1994;50:17953.
[50] Kresse G, Joubert D. Phys Rev B 1999;59:1758.
[51] Siegel DJ, Hector Jr LG, Adams JB. Acta Mater 2002;50:619.
[52] Saimoto S, Jin H. Mater Sci For 2007;550:339.
[53] Beeri O, Dunand DC, Seidman DN. Mater Sci Eng A 2010;527:3501.
[54] Dregia SA, Wynblatt P. Acta Metall Mater 1991;39:771.
[55] Hellman OC, Seidman DN. Mater Sci Eng A 2002;327:24.
[56] Krakauer BW, Seidman DN. Acta Mater 1998;46:6145.
[57] Seidman DN. Annu Rev Mater Res 2002;32:235.
[58] Marquis EA, Seidman DN, Asta M, Woodward C. Acta Mater 2006;54:119.
[59] Marquis EA, Seidman DN. Surf Interf Anal 2004;36:559.
[60] Isheim DI, Gagliano MS, Fine ME, Seidman DN. Acta Mater 2006;54:841.
[61] The scientific papers of J. Willard Gibbs. New York: Dover; 1961.
[62] Cahn JW. In: Johnson WC, Blakely JM, editors. Interfacial segregation metals park. OH: American Society of Metals; 1979. p. 3–38.
[63] Sutton AP, Balluffi RW. Interfaces in crystalline materials. Oxford: Clarendon Press; 1996. p. 349.
[64] Siegel DJ, Hamilton JC. Phys Rev B 2003;68:094105.
[65] Siegel DJ, van Schilfgaarde M, Hamilton JC. Phys Rev Lett 2004;92:086101.
[66] Siegel DJ. Appl Phys Lett 2005;87:121901.
[67] Landa A, Wynblatt P, Siegel DJ, Adams JB, Mryasov ON, Liu X-Y. Acta Mater 2000;48:1753.
[68] Siegel DJ, Hamilton JC. Acta Mater 2005;53:87.
[69] Siegel DJ, Hector LG, Adams JB. Surf Sci 2002;498:321.
[70] Benedek R, van de Walle A, Gerstl SSA, Asta M, Seidman DN. Phys Rev B 2005;71:094201.
[71] Siegel DJ, Hector Jr LG, Adams JB. Surf Sci 2002;498:321–36.
[72] Mehrer H, editor. Diffusion in solid metals and alloys, vol. 26. Berlin: Springer-Verlag; 1990.
[73] Cloutier C, Reeber-Schmansky P, Jones JW, Allison JE. Automotive alloys III. Warrendale, PA: TMS; 1999.
[74] Cloutier C, Jones JW, Allison JE. SAE paper 2000–01-0759. Warrendale, PA: SAE International; 1998.
[75] Mitlin D, Radmilovic V, Morris Jr JW. Metall Mater Trans A 2000;31A:2697.
[76] Haasen P. Physical metallurgy. New York: Press Syndicate of the University of Cambridge; 1996. p. 220.
[77] Hornbogen E. Aluminium 1967;43:115.
[78] Christian JW. The theory of transformations in metals and alloys. Oxford: Pergamon Press; 1981.
[79] Defay R, Prigogine I, Bellemans A, Everett DH. Surface tension and adsorption. New York: Wiley; 1966. p. 89.
[80] Krakauer BW. PhD thesis, Northwestern University; 1993.
[81] Seidman DN, Krakauer BW, Udler D. J Phys Chem Solids 1994;55:1035.
[82] Marquis EA. PhD thesis, Northwestern University; 2002. <http://arc.nucapt.northwestern.edu/refbase/show.php?record=151>.
[83] Krug ME, Dunand DC, Seidman DN. Acta Mater 2011;59:1700.
[84] Adusumilli P, Seidman DN, Murray CE; submitted for publication.
[85] Matsuda K, Teguri D, Uetani Y, Sato T, Ikeno S. Scr Mater 2002;47:833.
[86] Arnberg L, Aurivillius B. Acta Chem Scand A 1980;34:1.
[87] Phragmen G. J Inst Met 1950;77:489.
[88] Mondolfo LF. Aluminum alloys—structure and properties. London: Butterworths; 1976.
[89] Wolverton C. Acta Mater 2001;49:3129.